

ISTANBUL TECHNICAL UNIVERSITY ★ GRADUATE SCHOOL OF SCIENCE
ENGINEERING AND TECHNOLOGY

MICROWAVE IMAGING OF BRAIN STROKES



M.Sc. THESIS

İsmail DİLMAN

Department of Electronics and Communication

Telecommunication Engineering

DECEMBER 2016

ISTANBUL TECHNICAL UNIVERSITY ★ GRADUATE SCHOOL OF SCIENCE
ENGINEERING AND TECHNOLOGY

MICROWAVE IMAGING OF BRAIN STROKES



M.Sc. THESIS

İsmail DİLMAN
(504131343)

Department of Electronics and Communication

Telecommunication Engineering

Thesis Advisor: Assoc. Prof. Mehmet ÇAYÖREN

DECEMBER 2016

İSTANBUL TEKNİK ÜNİVERSİTESİ ★ FEN BİLİMLERİ ENSTİTÜSÜ

BEYİN KANAMALARININ MİKRODALGA GÖRÜNTÜLENMESİ

YÜKSEK LİSANS TEZİ

**İsmail DİLMAN
(504131343)**

Elektronik ve Haberleşme Mühendisliği Anabilim Dalı

Telekominikasyon Programı

Tez Danışmanı: Doç. Dr. Mehmet ÇAYÖREN

ARALIK 2016

İsmail Dilman, a M.Sc. student of ITU Graduate School of Science Engineering and Technology student ID 504131343, successfully defended the thesis/dissertation entitled “MICROWAVE IMAGING OF BRAIN STROKES”, which he prepared after fulfilling the requirements specified in the associated legislations, before the jury whose signatures are below.

Associate Prof. Mehmet ÇAYÖREN

Thesis Advisor : **Associate Prof. Mehmet ÇAYÖREN**
İstanbul Technical University

Jury Members: **Prof. Dr. Name SURNAME**
İstanbul Technical University

Prof. Dr. Name SURNAME

Prof. Dr. Name SURNAME

(If exists) **Prof. Dr. Name SURNAME**

(If exists) **Prof. Dr. Name SURNAME**

Date of Submission : 25 November 2016

Date of Defense :





To my parents



FOREWORD

This master thesis, where written during the time-period from Spring 2016 until Autumn 2016, under the teaching supervision of Prof. Mehmet ÇAYÖREN, İstanbul Technical University.

The intent of the thesis is to examine feasibility of microwave imaging based on contrast source inversion method to recognize the brain strokes.

I would like to thank the all the people who helped me in this thesis. Prof. Dr. İbrahim Akduman, who gave me the opportunity and confidence to work with the project, my thesis Advisor Associate Prof. Mehmet ÇAYÖREN for his suggestions, encouragements and guidance in writing the thesis and approaching the different. I would also like to thank Mehmet Nuri Akıncı and Dr. Egemen Bilgin from ITU ERG lab for their practical support, vision, and help.

Finally, I would like to thank my parents for their constant support during the time I studied.

December 2016

İsmail DİLMAN
B.Sc. Electronics and
Communication Engineering

TABLE OF CONTENTS

	<u>Page</u>
FOREWORD	ix
TABLE OF CONTENTS	xi
ABBREVIATIONS	xiii
SYMBOLS	xv
LIST OF TABLES	xvii
LIST OF FIGURES	xix
SUMMARY	xxiii
ÖZET	xxv
1. INTRODUCTION – MAIN TITLES(FIRST LEVEL TITLE)	1
1.1 Purpose of Thesis	2
1.2 Literature Review	2
1.3 Main Contributions	4
2. FORWARD SCATTERING PROBLEM	7
2.1 Derivation of 2D Helmholtz Equation	7
2.3 Discretization and Solution	13
3. INVERSE PROBLEM	17
3.1 Contrsat Source Inversion Method	17
3.2 Theoretical Background Contrast Source Inversion Method	19
3.2.1 Contrast source updating steps	20
3.2.2 Contrast updating steps	23
3.2.3 Initial values of contrast source inversion method	26
4. NUMERICAL RESULTS	29
4.1 Simulation Setup	29
4.2 Results of Contrast Source Alghorithm (Pozitive Constrait)	31
4.3 Results of Contrast Source Alghorithm (No Pozitive Constrait)	41
4.4 Results Of Differantial Imaging With Contrast Source Alghorithm (No Pozitive Constrait)	58
5. CONCLUSION	67
REFERENCES	71
CURRICULUM VITAE	74



ABBREVIATIONS

CSI	: Contrast Source Inversion
Mom	: Method of Moments
MHz	: Megahertz
GHz	: Gigahertz





SYMBOLS

t	: Time
\mathbf{E}, \mathbf{u}	: Field Vectors
ω	: Angular velocity
σ	: Conductivity
ϵ_r	: Dielectric constant





LIST OF TABLES

	<u>Page</u>
Table 4.1: 2nd Order Debye parameters for different types tissues.....	29





LIST OF FIGURES

	<u>Page</u>
Figure 4.1 : Measurement system configuration.....	30
Figure 4.2 : Electrical properties of head phantom (real part of contrast).....	31
Figure 4.3 : Electrical properties of head phantom (imaginary part of contrast part).....	31
Figure 4.4 : Electrical properties of head phantom (absolute value of contrast).....	32
Figure 4.5 : Real part of contrast on Microwave imaged by CSI algorithm of the phantom with 500Mhz operation frequency	33
Figure 4.6 : Imaginary part of contrast on Microwave imaged by CSI algorithm of the phantom with 500Mhz operation frequency	33
Figure 4.7 : Absolute value of contrast on Microwave imaged by CSI algorithm of the phantom with 500Mhz operation frequency.....	34
Figure 4.8 : Real part of contrast on Microwave imaged by CSI algorithm of the phantom with 800Mhz operation frequency	34
Figure 4.9 : Imaginary part of contrast on Microwave imaged by CSI algorithm of the phantom with 800Mhz operation frequency	35
Figure 4.10 : Absolute value of contrast on Microwave imaged by CSI algorithm of the phantom with 800Mhz operation frequency	35
Figure 4.11 : Real part of contrast on Microwave imaged by CSI algorithm of the phantom with 1GHz operation frequency.....	36
Figure 4.12 : Imaginary part of contrast on Microwave imaged by CSI algorithm of the phantom with 1GHz operation frequency.....	36
Figure 4.13 : Absolute value of contrast on Microwave imaged by CSI algorithm of the phantom with 1GHz operation frequency.....	36
Figure 4.14 : Real part of contrast on Microwave imaged by CSI algorithm of the phantom with 1.2GHz operation frequency.....	37
Figure 4.15 : Imaginary part of contrast on Microwave imaged by CSI algorithm of the phantom with 1.2GHz operation frequency.....	37
Figure 4.16 : Absolute of contrast on Microwave imaged by CSI algorithm of the phantom with 1.2GHz operation frequency.....	38
Figure 4.17 : Electrical properties of head phantom with different centered blooded area (real value of contrast	38
Figure 4.18 : Real part of contrast on Microwave imaged by CSI algorithm of the phantom with 1GHz operation frequency.....	39
Figure 4.19 : Imaginary part of contrast on Microwave imaged by CSI algorithm of the phantom with 1GHz operation frequency.....	39
Figure 4.20 : Absolute value of contrast on Microwave imaged by CSI algorithm of the phantom with 1GHz operation frequency.....	39
Figure 4.21 : Electrical properties of head phantom without matching medium (real value of contrast)	40
Figure 4.22 : Real part of contrast on Microwave imaged by CSI algorithm of the phantom with 500MHz operation frequency and without matching medium.....	40

Figure 4.23 : Absolute value of contrast on Microwave imaged by CSI algorithm of the phantom with 500MHz operation frequency and without matching medium.....	41
Figure 4.24 : Imaginary part of contrast on Microwave imaged by CSI algorithm of the phantom with 500MHz operation frequency and without matching medium.....	41
Figure 4.25 : Electrical properties of head phantom with matching medium (real value of contrast)	42
Figure 4.26 : Real part of contrast on Microwave imaged by CSI algorithm of the phantom with 500MHz operation frequency and with matching medium $\epsilon_b = 20$	43
Figure 4.27 : Imaginary part of contrast on Microwave imaged by CSI algorithm of the phantom with 500MHz operation frequency and with matching medium $\epsilon_b = 20$	43
Figure 4.28 : Absolute value of contrast on Microwave imaged by CSI algorithm of the phantom with 500MHz operation frequency and with matching medium $\epsilon_b = 20$	43
Figure 4.29 : Real part of contrast on Microwave imaged by CSI algorithm of the phantom with 800MHz operation frequency and with matching medium $\epsilon_b = 20$	44
Figure 4.30 : Imaginary part of contrast on Microwave imaged by CSI algorithm of the phantom with 800MHz operation frequency and with matching medium $\epsilon_b = 20$	44
Figure 4.31 : Absolute value of contrast on Microwave imaged by CSI algorithm of the phantom with 800MHz operation frequency and with matching medium $\epsilon_b = 20$	45
Figure 4.32 : Real part of contrast on Microwave imaged by CSI algorithm of the phantom with 1GHz operation frequency and with matching medium $\epsilon_b = 20$	45
Figure 4.33 : Imaginary part of contrast on Microwave imaged by CSI algorithm of the phantom with 1GHz operation frequency and with matching medium $\epsilon_b = 20$	46
Figure 4.34 : Absolute value of contrast on Microwave imaged by CSI algorithm of the phantom with 1GHz operation frequency and with matching medium $\epsilon_b = 20$	46
Figure 4.35 : Real part of contrast on Microwave imaged by CSI algorithm of the phantom with 1.2GHz operation frequency and with matching medium $\epsilon_b = 20$	47
Figure 4.36 : Imaginary part of contrast on Microwave imaged by CSI algorithm of the phantom with 1.2GHz operation frequency and with matching medium $\epsilon_b = 20$	47
Figure 4.37 : Absolute value of contrast on Microwave imaged by CSI algorithm of the phantom with 1.2GHz operation frequency and with matching medium $\epsilon_b = 20$	47
Figure 4.38 : Real part of contrast on Microwave imaged by CSI algorithm of the phantom with 500MHz operation frequency and with matching medium $\epsilon_b = 40$	48
Figure 4.39 : Imaginary part of contrast on Microwave imaged by CSI algorithm of the phantom with 500MHz operation frequency and with matching medium $\epsilon_b = 40$	48

Figure 4.40 : Absolute value of contrast on Microwave imaged by CSI algorithm of the phantom with 500MHz operation frequency and matching medium $\epsilon_b = 40$	49
Figure 4.41 : Real part of contrast on Microwave imaged by CSI algorithm of the phantom with 800MHz operation frequency and with matching medium $\epsilon_b = 40$	49
Figure 4.42 : Imaginary part of contrast on Microwave imaged by CSI algorithm of the phantom with 800MHz operation frequency and with matching medium $\epsilon_b = 40$	50
Figure 4.43 : Absolute value of contrast on Microwave imaged by CSI algorithm of the phantom with 800MHz operation frequency and with matching medium $\epsilon_b = 40$	50
Figure 4.44 : Real part of contrast on Microwave imaged by CSI algorithm of the phantom with 1GHz operation frequency and with matching medium $\epsilon_b = 40$	51
Figure 4.45 : Imaginary part of contrast on Microwave imaged by CSI algorithm of the phantom with 1GHz operation frequency and with matching medium $\epsilon_b = 40$	51
Figure 4.46 : Absolute value of contrast on Microwave imaged by CSI algorithm of the phantom with 1GHz operation frequency and with matching medium $\epsilon_b = 40$	51
Figure 4.47 : Real part of contrast on Microwave imaged by CSI algorithm of the phantom with 1.2GHz operation frequency and with matching medium $\epsilon_b = 40$	52
Figure 4.48 : Imaginary part of contrast on Microwave imaged by CSI algorithm of the phantom with 1.2GHz operation frequency and with matching medium $\epsilon_b = 40$	52
Figure 4.49 : Absolute value of contrast on Microwave imaged by CSI algorithm of the phantom with 1.2GHz operation frequency and with matching medium $\epsilon_b = 40$	53
Figure 4.50 : Real part of contrast on Microwave imaged by CSI algorithm of the phantom with 500MHz operation frequency and with matching medium $\epsilon_b = 60$	53
Figure 4.51 : Imaginary part of contrast on Microwave imaged by CSI algorithm of the phantom with 500MHz operation frequency and with matching medium $\epsilon_b = 60$	54
Figure 4.52 : Absolute value of contrast on Microwave imaged by CSI algorithm of the phantom with 500MHz operation frequency and with matching medium $\epsilon_b = 60$	54
Figure 4.53 : Real part of contrast on Microwave imaged by CSI algorithm of the phantom with 800MHz operation frequency and with matching medium $\epsilon_b = 60$	55
Figure 4.54 : Imaginary part of contrast on Microwave imaged by CSI algorithm of the phantom with 800MHz operation frequency and with matching medium $\epsilon_b = 60$	55
Figure 4.55 : Absolute value of contrast on Microwave imaged by CSI algorithm of the phantom with 800MHz operation frequency and with matching medium $\epsilon_b = 60$	55

Figure 4.56 : Real part of contrast on Microwave imaged by CSI algorithm of the phantom with 1GHz operation frequency and with matching medium $\epsilon_b = 60$	56
Figure 4.57 : Imaginary part of contrast on Microwave imaged by CSI algorithm of the phantom with 1GHz operation frequency and with matching medium $\epsilon_b = 60$	56
Figure 4.58 : Absolute value of contrast on Microwave imaged by CSI algorithm of the phantom with 1GHz operation frequency and with matching medium $\epsilon_b = 60$	57
Figure 4.59 : Real part of contrast on Microwave imaged by CSI algorithm of the phantom with 1.2GHz operation frequency and with matching medium $\epsilon_b = 60$	57
Figure 4.60 : Imaginary part of contrast on Microwave imaged by CSI algorithm of the phantom with 1.2GHz operation frequency and with matching medium $\epsilon_b = 60$	57
Figure 4.61 : Absolute value of contrast on Microwave imaged by CSI algorithm of the phantom with 1.2GHz operation frequency and with matching medium $\epsilon_b = 60$	58
Figure 4.62 : Zubal Phantom model for growing blood regions, real value of the actual contrast function for the first measurement.....	59
Figure 4.63 : Zubal Phantom model for growing blood regions, real value of the actual contrast function for the second measurement.....	59
Figure 4.64 : Real value of reconstruction of the differential contrast function $\delta\chi(r)$ in the case of growing blood regions.....	60
Figure 4.65 : Imaginary value of reconstruction of the differential contrast function $\delta\chi(r)$ in the case of growing blood regions.....	60
Figure 4.66 : Absolute value of reconstruction of the differential contrast function $\delta\chi(r)$ in the case of growing blood regions.....	61
Figure 4.67 : Real value of reconstruction of the differential contrast function $\delta\chi(r)$ in the case of growing blood regions.....	62
Figure 4.68 : Imaginary value of reconstruction of the differential contrast function $\delta\chi(r)$ in the case of growing blood regions.....	62
Figure 4.69 : Absolute value of reconstruction of the differential contrast function $\delta\chi(r)$ in the case of growing blood regions.....	62
Figure 4.70 : Zubal Phantom model for mixed case, real value of the actual contrast function $\chi(r)$,for the first measurement.....	63
Figure 4.71 : Zubal Phantom model for mixed case, real value of the actual contrast function $\chi(r)$,for the second measurement.....	64
Figure 4.72 : Real value Reconstruction of the differential contrast function $\delta\chi(r)$ for mixed case.....	64
Figure 4.73 : Imaginary value Reconstruction of the differential contrast function $\delta\chi(r)$ for mixed case.....	65
Figure 4.74 : Absolute value Reconstruction of the differential contrast function $\delta\chi(r)$ for mixed case.....	65
Figure 4.75 : Absolute value Reconstruction of the differential contrast function $\delta\chi(r)$ for static case.....	66

MICROWAVE IMAGING FOR BIOLOGICAL ISSUES

SUMMARY

This thesis investigates feasibility of detection and continuous monitoring of hemorrhagic brain strokes in a realistic head phantom with microwave imaging. The head phantom is illuminated by 36 line sources and the scattering field data is calculated numerically with method of moments for each scenarios. Additive white Gaussian noise with minimum level 30 dB SNR is added for scenarios that are more realistic. Two different approaches are used for detection and continuous monitoring of blood region. In first approach, contrast source inversion method is used to reconstruct the blood region. Scattering fields' data that are obtained by a simulation on matlab platform at different frequencies from 500 MHz to 1.2 GHz is used for only input parameters for CSI method. No any other priory information is used. Moreover, results with either electrically different background mediums or free space are discussed in this approach. The numerical results show that it is possible to determine the square shape blooded area with size about 2.6cm x 2.6cm between the 800-1000 MHz frequency ranges in the dielectric-matching medium. In second approach, CSI method is used to reconstruction again except the input parameters scattering field data is replaced with differential data, which is the difference of two scattering fields' data. These scattering fields' data's are obtained in two different times. Hence, reconstruction contains of changes in multiple blood regions and provides information about the locations instead of all domain reconstruction. Here, aim is to determine the change of bleeding in sequential time frames. The numerical results show that it is possible to monitor the changes in the blood regions within the human brain, if optimal values of matching medium are chosen.



BİYOLOJİK DOKULARIN MİKRODALGA GÖRÜNTÜLENMESİ

ÖZET

Günümüzde biyolojik dokuların zararsız bir şekilde görüntülenmesinde yeni bir yaklaşım olan mikrodalga görüntüleme tekniklerinin önemi artmaktadır. Özellikle tıp alanında, medikal görüntülemelerde alışla gelmiş yöntemler çeşitli dezavantajlar içermektedir. Örneğin manyetik rezonans görüntüleme (MRI) oldukça pahalı bir yöntem iken, X-ray uygulama esnasında içerdiği iyonize radyasyon ile sağlık riski oluşturmaktadır. Bilgisayarlı tomografi ise (CT) yumuşak dokuların görüntülenmesinde etkili sonuç vermemektedir. Pozitron emisyon tomografi diğer yöntemlere göre düşük çözünürlük sağlamaktadır. Ayrıca tüm bu yöntemlerin taşınabilirliği de mümkün değildir. Alışla gelmiş bu yöntemlerin bahsi geçen dezavantajlarından dolayı mikrodalga görüntülemenin alternatif olabileceği düşüncesinden yola çıkarak bu tez çalışması gerçekleştirildi. Mikrodalga görüntüleme yöntemi olarak contrast source inversion method seçildi ve seçilen bu yöntem beyin kanaması geçirdiği varsayılan gerçekçi insan kafa modeli üzerinde simülasyon ortamında denendi. Kanama gerçekleşen bölgenin mikrodalga temelli görüntülenmesinde contrast source inversion algoritması esas alınarak iki farklı yaklaşım gerçekleştirilmiştir. Contrast source inversion algoritması için gerekli veri seti olarak Zubal fantom modellerinden MRI kafa modeli kullanıldı. Zubal fantom 3-D kafa modeli olup, üst üste dizilmiş 128 adet enine kesitten oluşmaktadır. Bu tez çalışmasında kafanın üst kısmı olan, beyin bölgesini içeren üstten bakıldığında 48.kesit mikrodalga görüntülemenin yapılacağı düzlem olarak seçilmiştir. Orjinal zubal fantom modelinin her kesiti 256x256 boyutlarında matrislerden oluşmakta iken hesaplama zamanını ve maliyetini azaltmak amacıyla seçilen kesit 140x190 boyutlarına kadar küçültülmüştür. Bu küçültme işleminde kafa ve beyin bölgesini içermeyen datalar elemine edilmiştir. Zubal modeli gerçekçi bir kafa modeli olarak çok fazla doku içermektedir. Bu çalışmada sadece en fazla hacim kaplayan 8 farklı doku ele alınmıştır. Bu dokular genel itibarıyla kafanın içinden dışarı doğru sırasıyla

deri, kafatası, yağ, serebrospinal sıvı (CSF), sert zar (Dura), gri madde, beyaz madde ve görüntülenmek istenen eklenmiş kanlı dokudur. Zubal fantom modelinde dokular data setinde indis numaralarıyla temsil edilmektedir. Bu şekilde mikrodalga görüntülemeye kullanılmaları mümkün değildir. Bu sebeple her bir dokunun indis numaraları dokuların elektriksel özelliklerini temsil eden dielektrik katsayıları ve iletkenlik değerleri ile değiştirilmiştir. Dokuların dielektrik katsayıları ve iletkenlik değerleri 2.dereceden Debye modeli kullanılarak elde edilmiştir. Son olarak oluşturulan beyin modeli üzerinde seçilen bir yere kanamalı bölgeyi temsilen kan bloğu yerleştirilmiştir. Zubal fantom, görüntülemenin yapılacağı kenar uzunluğu 17cm olan karesel bir bölgeye yerleştirilmiştir. Bu karesel bölge 195x195 boyutlarında matris şeklinde matlab ortamında oluşturulmuştur. Kafa veya beyine ait olmayan matris elemanlarına görüntülemenin yapılacağı ortama ait dielektrik parametresi eklenmiştir. Zubal fantom, etrafına merkezden 15cm uzaklıktaki noktalara 10 derece aralıklarla (36 adet) yerleştirilen çizgisel kaynak şeklindeki antenler sistemi ile aydınlatmaktadır. Aynı antenler saçılan alanın hesaplandığı noktalar olarak da seçilmiş ve 36x36 boyutunda saçılma matrisi oluşturulmuştur. Saçılan alan matrisi method of moments yöntemiyle numerik olarak hesaplanmıştır. Hesaplanan saçılan alan matrisine gerçek hayattaki uygulamalar düşünülerek en az 30dB seviyesinde Additive white Gaussian tipinde gürültü eklenmiştir. Birinci yaklaşımda düz problemin çözümünden elde edilen saçılan alan matrisi contrast source inversion methodu için giriş parametresi olarak kullanıldı ve kanlı bölge eklenmiş zupal kafa modeli iteratif bir şekilde tekrar oluşturuldu. Boyutları 2.6cm x 2.6cm olan kare şeklindeki kan bloğu içeren zupal kafa fantomu, dielektrik özelliği 20 olan hesaplama uzayında görüntülendi. Ayrıca görüntülenme düzlemi 17cm x 17cm boyutlarında bir kare olup, bu düzlem 65x65 adet hücreye bölündü. Böylece düz ve ters problemde farklı hücre boyutları kullanılmış oldu. Çalışma frekansı olarak 500MHz, 800MHz, 1GHz ve 1.2GHz seçildi. Daha yüksek frekanslarda elektromagnetik dalgaların zupal kafa modelinin içine teneffüs etmemesinden dolayı görüntüleme gerçekleştirilemedi. 500MHz den daha düşük frekanslar, anten boyu gerçekleştirilebilir uygulamalarda kullanılabilecek sınırların üstüne çıktığı için incelemeye alınmadı. Matematiksel olarak çok doğru bir yaklaşım olmasada mikrodalga görüntüleme algoritmasında her iterasyonda sonuçlara pozitif zorlama uygulandı. 500MHz ve 800MHz frekanslarında 2.6cmx2.6cm şeklindeki kan bloğu, konum ve boyut olarak oldukça doğru bir biçimde görüntülendi. 1Ghz frekansında

ise çözünürlük yükseldi, kafaya ve beyine ait dokular daha net belirginleşti fakat kanlı bölge net bir şekilde gözlemlenemedi. 1.2 Ghz frekansında ise kanlı bölgenin görüntülenmesi adına anlamlı sonuçlar elde edilemedi. Aynı yaklaşım pozitif zorlama olmadan da gerçekleştirildi. Bu durumda kafanın sınırları daha net bir şekilde belirlenirken, sadece 500MHz de kan blogu görüntülenebildi. Ayrıca görüntülemenin yapıldığı uzayın dielektrik katsayısı 30 olarak belirlendi. Kan blogu kafa modeli içerisinde farklı konumlara konuldu ve yöntemin değişen konumlara göre tutarlı sonuç verdiği görüldü. Dış uzayın dielektrik içermemesi yani boş uzay olması durumunda mikrodalga görüntülemenin mümkün olmadığı görüldü. Bu durum seçilen mikrodalga yönteminin gerçek hayatta uygulanması için matching medium kullanılması gerekliliğini ortaya koydu. İkinci yaklaşımda mikrodalga görüntüleme yöntemi olarak seçilen contrast source inversion algoritmasına giriş parametresi olarak iki farklı zamanda hesaplanan saçılan alanların farkı uygulandı. Bu yöntemde amaçlanan kan blogunun değişimini gözlemlemektir. Yöntemin tutarlılığını test etmek adına dört farklı seneryo simule edildi. İlk seneryoda 1.4cm x 1.4cm kan blogu eklenmiş fantomdan saçılan alan hesaplandı Daha sonra bu kan blogunun boyutu 2.6cm x 2.6cm getirilmiş ve kafanın başka bir bölgesine daha 1.4cm x 1.4cm boyutlarında kan blogu eklendi. İkinci durum için de saçılan alan hesaplandıktan sonra bu iki saçılan alan matrisinin farklı alınıp contrast source algoritmasına giriş parametresi olarak uygulandı. Ayrıca her bir saçılan alan matrisine 30dB seviyesinde Additive white Gaussian tipinde gürültü eklendi. Contrast source inversion algoritması herhangi bir değişiklik yapılmaksızın uygulandı. Contrast source inversion algoritma temelli mikrodalga görüntüleme sonucunda büyüyen ve yeni oluşan kan blokları net bir şekilde 500MHz çalışma frekansında tespit edildi. Kafanın ve beynin diğer dokuları hakkında ise yöntemin dogası gereği herhangi bir fikir elde edilemedi. İkinci senaryoda ilk seneryonun tam tersi uygulandı. Sonuç olarak kan blogunun küçüldüğü ve yok olduğu yerlerde negatif kontrast elde edildi ve değişim net bir şekilde tespit edildi. Üçüncü seneryoda ilk iki seneyonun bir nevi aynı anda olduğu durum simule edildi. Büyüyen kan blogunun olduğu yerlerde yüksek kontrast ve küçülen kan blogunun olduğu yerlerde negatif kontrast elde edildi. En son seneryoda ise değişmeyen durum göz önüne alındı ve sadece ölçümlere eklenen gürültülerin farkı gözlemlendi.



1. INTRODUCTION

Microwave imaging techniques constitute an important research subject in the field of non-destructive imaging of biological tissues. These techniques provide alternatives to the established medical imaging methods such as X-rays, magnetic resonance imaging (MRI), computed tomography (CT), or positron emission tomography (PET). Although they have been effectively used in the detection of tumors, bone fractures, etc.; these conventional techniques have some drawbacks such as high implementation cost for MRI or additional health risks due to ionizing radiation for X-rays [1]. Moreover, there are performance limitations for each technique. For instance, CT provides limited information about soft tissues, whereas PET has a low spatial resolution compared to the alternative methods [2]. In addition, it should be noted that those systems are usually expensive, require high infra-structural costs, and they are non-portable.

Therefore, it can be suggested that new techniques can make meaningful contributions to the field of medical imaging. Microwave imaging techniques rely on the difference of the electromagnetic parameters between different biological tissues [3]. When an external electromagnetic source operating in microwave frequencies is used to excite a biological target, this difference in the electromagnetic parameters produces a variation in the scattered field. This measured scattered field is used as the data of some inversion algorithm to reconstruct the human body organs, and to detect malign tissues. Through this approach, low-cost, non-hazardous, and possibly portable imaging devices can be designed [4]. A further advantage of these techniques would be an ability to monitor the state of the patients continuously [4]. It should be noted that for continuous monitoring the main aim is to detect the changes in the interior structure of the biological tissue. This a relatively simple task than reconstructing the entire interior structure; therefore, alternative algorithms, which are easier to implement, and require less computational effort, can be used for this task.

1.1 Purpose of Thesis

The main aim of this thesis is to develop a method for microwave imaging of hemorrhagic brain stroke that is to detect blood regions within the human brain via measurement of the scattered field. Brain stroke is one of the most common sources of death in the globe, and for most of the cases, the survivors have to live with permanent or long time disabilities [3-5]. Conventional techniques such as MRI, are usually effective for early detection, however they are not suitable for continuous monitoring of the stroke affected patients.

Therefore, this work has two related but different objectives. First, to develop a quantitative imaging algorithm whose aim is to reconstruct the electromagnetic parameters of the entire brain region. Since each tissue has different electromagnetic parameter, this algorithm would ideally produce a map of the brain of the patient. Because of the complexity of the human brain, this is a challenging task, and only an approximation of the actual brain structure can be obtained. Nevertheless, it will be demonstrated that this approach can be used to detect relatively large stroke regions accurately.

The second objective of the thesis is to develop a technique that detects the changes in the brain of the patients. Since these changes will be caused by the shrinking or growing blood regions, this approach is especially suitable for the continuous monitoring of the stroke affected patients. Here, the aim is solely to detect the exact locations of the changes. As this does not involve an actual reconstruction of the electromagnetic parameters, the computational effort needed for the task will be much less than the previous case. This technique can be named as differential imaging of the human brain.

1.2 Literature Review

Various applications of the microwave imaging techniques for different tissues such as breast [6], bone [7], or heart [8] can be found in the literature. All the applications rely on the difference of electromagnetic parameters between healthy tissues and malignant tissues, and include a suitable inversion algorithm. However, depending

on the aim of the algorithms the microwave imaging techniques can be classified into two main groups as qualitative and quantitative techniques. Qualitative methods provide information about the shapes and the locations of the scattering objects within the domain. Techniques such as linear sampling method [9], factorization method [10], or point source method [11] are examples of qualitative imaging techniques. Although they have high computational efficiency, these techniques cannot be used to reconstruct the electromagnetic parameters of the scatterers. Therefore, they are more suitable for differential imaging that is continuous monitoring. On the other hand, the quantitative techniques, which are computationally expensive, can be employed to reconstruct the dielectric profile of the scatterer, that is, they provide both the shape and the electromagnetic parameters of the objects. Well-known quantitative techniques such as Newton-Kantorovich method [12], Levenberg-Marquadt method [13], or distorted Born iterative method [14] are used for medical imaging applications.

Brain stroke detection is a particularly challenging problem for microwave imaging. The main reason is the complexity of the human brain compared to more homogeneous tissues such as breast. Moreover, the contrast between the electromagnetic parameters of the human blood and brain tissues such as cerebrospinal fluid is not very high. Also, the existence of the human skull makes the penetration of the electromagnetic parameters into the inner region of the brain more difficult. Nevertheless, different techniques have been employed for the stroke detection [4, 15-17]. In [4], a Newton-based iterative scheme has been used, whereas in [15] the Born iterative method has been employed. On the other hand, in [16] and in [17], qualitative techniques are used to detect stroke areas. In [18], the performance of multiplicative regularized contrast source inversion method has been analyzed on a biological model. Moreover, 3-D application of the same approach is presented in [19] using a simple model.

For differential imaging, a few alternatives have been proposed in the existing literature. In [20], truncated singular value decomposition method is used in the differential imaging. The same technique is demonstrated on a homogeneous brain model in [21]. The method is shown to be capable of detecting the region of change for low noise levels. In [22], a study with a realistically head model demonstrates that for ultra wide band magnitude combined tomography algorithm, differential

imaging produces better results than the direct application. These works demonstrate that the main limitation of the differential techniques is the sensitivity to the noise in the measurement of the scattered field.

1.3 Main Contributions

In this thesis, the feasibility of a microwave imaging technique for the detection of hemorrhagic brain stroke has been investigated. The technique is based on the well-known contrast source inversion algorithm [23], which relies on the minimization of a cost function composed of the errors in the data and the object equations of the inverse scattering problem. For the head model, a 2-D realistically head model, which includes most of the brain tissues including the cerebrospinal fluid is used. The brain is assumed to be excited by ideal line sources situated on a circle outside the measurement domain. The scattered field, which is synthetically produced via method of moments, is assumed to be measured on the same circular region. Using the scattered field as the data of the contrast source inversion algorithm, the electromagnetic parameters of the brain region are obtained.

In the case of full reconstruction, the method yields an approximation of the actual head model. Nevertheless, it is observed that reconstructed profile indicates the locations and sizes of the blood regions, if a suitable operating frequency is chosen. Apart from the frequency, another important factor that determines the success of the reconstruction algorithm is the matching medium. A matching medium minimizes the reflection in the interface between human head and the air, and therefore increases the penetration of the electromagnetic field into the inner regions of the brain. Various numerical simulations have been performed to test the performance of the method, and the effect of the parameters such as the frequency or the dielectric parameter of the matching medium. The results demonstrate that even with additive Gaussian noise in the scattered field, the method can be used to locate stroke areas of reasonable sizes within the human brain.

For differential imaging, a similar algorithm based on the contrast source inversion technique is employed. In this case, the difference between the scattered fields measured in different time steps is used as the data of the inversion algorithm. Through this procedure, a differential contrast function is obtained instead of the actual values of the dielectric profile. Due to the non-linearity of the inverse problem,

this differential contrast function does not correspond to the actual difference in the electromagnetic parameters between two measurements of the scattered field. Nevertheless, it has been observed that the method accurately locate the growing or shrinking blood regions. Moreover, the differential imaging algorithm is capable of detecting the relatively small changes that go unnoticed in the full reconstruction scheme. The toleration for the noise level is also strong compared to the techniques available in the literature. Overall, it can be concluded that the method provides a good alternative to the techniques available in the literature for the field of microwave imaging, and it can form a basis for practical medical applications in the future.





2. FORWARD SCATTERING PROBLEM

2.1 Derivation of 2D Helmholtz Equation

Let us start with the Maxwell's equations in time domain as indicated from (2.1) to (2.5):

$$\nabla \times \vec{E} = -\frac{\partial \vec{B}}{\partial t} - \vec{J}_{mv} \quad (2.1)$$

$$\nabla \times \vec{H} = \frac{\partial \vec{D}}{\partial t} + \vec{J}_{ev} \quad (2.2)$$

$$\nabla \cdot \vec{D} = \rho_v \quad (2.3)$$

$$\nabla \cdot \vec{B} = \rho_m \quad (2.4)$$

$$\vec{J}_{ev} = \sigma \vec{E} + \vec{J}_1 \quad (2.5)$$

We assume a time-harmonic dependence of $e^{-i\omega t}$, the phasor form of the Maxwell's equations becomes as indicated from (2.6) to (2.9):

$$\nabla \times \vec{E} = j\omega\mu\vec{H} - \vec{J}_{mv} \quad (2.6)$$

$$\nabla \times \vec{H} = -j\omega\epsilon\vec{E} + \sigma\vec{E} + \vec{J}_1 \quad (2.7)$$

$$\nabla \cdot \vec{D} = \rho_v \quad (2.8)$$

$$\nabla \cdot \vec{B} = \rho_m \quad (2.9)$$

To derive the Helmholtz equation we have to take rotational of Faraday's and Ampere's law as indicated (2.10) and (2.11):

$$\nabla \times \nabla \times \vec{E} = j\omega\mu \nabla \times \vec{H} - \nabla \times \vec{J}_{mv} \quad (2.10)$$

$$\nabla \times \nabla \times \vec{H} = -j\omega\epsilon \nabla \times \vec{E} + \nabla \times (\sigma \vec{E} + \vec{J}_1) \quad (2.11)$$

Then by using the identity as indicated (2.12):

$$\nabla \times \nabla \times \vec{f} = \nabla(\nabla \cdot \vec{f}) - \nabla^2 \vec{f} \quad (2.12)$$

we transform the above equations into the Helmholtz equations as indicated (2.13) and (2.14):

$$\nabla^2 \vec{E} = \frac{\nabla \rho_{ev}}{\epsilon} - \omega^2 \epsilon \mu \vec{E} - j\omega\mu\sigma \vec{E} - j\omega\mu \vec{J}_1 + \nabla \times \vec{J}_{mv} \quad (2.13)$$

$$\nabla^2 \vec{H} = \frac{\nabla \rho_{mv}}{\epsilon} - \omega^2 \mu \epsilon \vec{H} - j\omega\epsilon \vec{J}_{mv} - \nabla \times \sigma \vec{E} - \nabla \times \vec{J}_1 \quad (2.14)$$

2.2 Derivation of 2D Green Equation

For a 2D transverse magnetic scattering case, where the scatterers are symmetric with respect to the z-axis and the electric field is parallel to z-axis, the Helmholtz equation above translates into a scalar form for which $u = E_z$ as indicated (2.15):

$$\nabla^2 u + k^2 u = 0 \quad (2.15)$$

Consider scattering scenario where the wave number distribution is indicated (2.16):

$$k^2(\vec{r}) = \begin{cases} \omega^2 \epsilon(\vec{r}) \mu_0 + i\omega\sigma(\vec{r})\mu_0, & \vec{r} \in \Omega \\ k_0^2, & \vec{r} \notin \Omega \end{cases} \quad (2.16)$$

Here the scatterer is confined in the region Ω and outside of this domain is filled with a specific background medium. Assuming the medium is excited with a plane wave illumination of u^i and the scattered field is defined by $u^s = u - u^i$, we can make the below manipulations from (2.17) to (2.20):

$$\nabla^2 u^s + \nabla^2 u^i + k^2 u^s + k^2 u^i = 0 \quad (2.17)$$

$$\nabla^2 u^s + \nabla^2 u^i + k^2 u^s + k^2 u^i + k_0^2 u^i + k_0^2 u^s - k_0^2 u^i - k_0^2 u^s = 0 \quad (2.18)$$

$$\nabla^2 u^s + k^2 u + k_0^2 u^s - k_0^2 u = 0 \quad (2.19)$$

$$\nabla^2 u^s + k_0^2 u^s = -u \left(\frac{k^2}{k_0^2} - 1 \right) k_0^2 \quad (2.20)$$

The above equation can be readily solved by evaluating the Green's function of a point source in the specific background. Suppose 2D green function is given equation (2.21):

$$G(x, y) = G(x_1, y_1; x_2, y_2) \quad (2.21)$$

x_1 and y_1 variables are coordiantes of observation points and x_2 and y_2 variables are source points as indicated (2.22) .

$$\nabla^2 G + k^2 G = -\delta(x_1 - x_2)\delta(y_1 - y_2) \quad (2.22)$$

Observation and source points can be defined in cylindrical coordinates like equation as (2.23) ('indices indicate source points)

$$x_1 = \rho \cos \phi \quad x_2 = \rho' \cos \phi' \quad y_1 = \rho \sin \phi \quad y_2 = \rho' \sin \phi' \quad (2.23)$$

Characterize properties of delta Dirac function is usable for solving equation. Integration from minus infinite-to-infinite gives one due to only one value on same point's source and observation. Equation (2.25) present the cylindrical coordinate of equation (2.24). In order to prevent unit solution inverse of metric coefficients is multiplied.

$$\iint_{-\infty}^{\infty} \delta(x_1 - x_2) \delta(y_1 - y_2) dx_1 dy_1 = 1 \quad (2.24)$$

$$\iint_{-\infty}^{\infty} \frac{1}{\rho'} \delta(\rho - \rho') \delta(\phi - \phi') \rho' d\rho' d\phi' = 1 \quad (2.25)$$

Let's source point type of delta Dirac on origin. Equation comes new form as indicated (2.26):

$$\vec{\rho}' = 0 \quad \nabla^2 G + k^2 G = -\frac{1}{\rho'} \delta(\rho) \delta(\phi) \quad [\rho' = 0] \quad (2.26)$$

Firstly, inhomogeneous differential equation without its right part is solved like homogenous equation as indicated (2.27):

$$\frac{1}{\rho} \frac{\partial}{\partial \rho} \left(\rho \frac{dG}{d\rho} \right) + k^2 G = 0 \quad (2.27)$$

Equation 2.27 is type of zero order Bessel differential equation. Solution of homogenous Bessel differential equations is given with unknown coefficients and Henkel functions as indicated (2.28):

$$G(\rho) = C_1 H_0^1(k\rho) + C_2 H_0^2(k\rho) \quad (2.28)$$

Asymptotic behavior of Henkel function is given at equation (2.29) while $k\rho$ is approaching to infinite. Zero order first kind Henkel function term states outgoing wave while zero order second kind function term state incoming wave (2.30). Second term, incoming wave is not physical meaningful.

$$H_0^1(k\rho) \rightarrow \frac{\sqrt{2} e^{ik\rho}}{\sqrt{\pi k\rho}} e^{-\frac{i\pi}{4}} \quad (2.29)$$

$$H_0^2(k\rho) \rightarrow \frac{\sqrt{2} e^{-ik\rho}}{\sqrt{\pi k\rho}} e^{\frac{i\pi}{4}} \quad (2.30)$$

$$\nabla^2 G + k^2 G = -\delta(\vec{\rho} - \vec{\rho}') \quad (2.31)$$

Gauss theorem is applied on equation (2.31) and right part comes to -one .Left part of the equations are separated two parts and calculated as indicated (2.32):

$$\int_B \nabla \cdot (\nabla G) dv + \int_B k^2 G dv = -1 \quad (2.32)$$

About the properties of gauss theorem volume integral return to surface integral as shown in equation (2.33):

$$\int_S \nabla G \cdot d\vec{s} + \int_B k^2 G dv = -1 \quad (2.33)$$

Green functions is $\vec{\rho}$ direction also perpendicular bottom and top surface as indicated (2.34):

$$\int_S \frac{\partial G}{\partial \rho} \cdot d\vec{s} + k^2 \int_B G dv = -1 \quad (2.34)$$

Green function derivative is calculated with equation (2.35):

$$\frac{dG}{d\rho} = C_1 \frac{d[H_0^1(k\rho)]}{d\rho} \quad (2.35)$$

First kind of Henkel function derivation is defined as indicated (2.36) and (2.37):

$$\frac{d[H_n^1(x)]}{dx} = \frac{nH_n^1(x)}{x} - H_{n+1}^1(x) \quad (2.36)$$

$$\frac{d[H_0^1(k\rho)]}{d\rho} = (-1)H_1^1(k\rho) \quad (2.37)$$

Gauss theorem used on unit length cylinder with radius ρ_0 and obtained equation (2.38):

$$\int_0^1 \int_0^{2\pi} (-1)C_1 H_1^1(k\rho_0) \rho_0 d\phi dx_s + k^2 \int_0^1 \int_0^{2\pi} \int_0^{\rho_0} C_1 H_0^1(k\rho) \rho d\rho d\phi dx_s = -1 \quad (2.38)$$

Zero order first kind Henkel function value is approaching infinite while its variable is zero. According to this solution second term of right part equation is zero and indicated as (2.39):

$$H_0^1(x) = \ln x \lim_{x \rightarrow 0} H_0^1(x) = \infty \quad (2.39)$$

N order first kind Henkel function is given in equation while its variable is zero indicated as (2.40):

$$\lim_{x \rightarrow 0} H_n^1(x) = -\frac{i(n-1)!}{\pi} \left(\frac{2}{x}\right)^n \quad n \geq 1 \quad (2.40)$$

After that when we set the equation 2.40 into integral equation 2.38, unknown coefficient C_1 is obtained as seen in equations (2.41) and (2.42):

$$\frac{(-1)C_1 k(i)0!}{\pi} \times \frac{2}{k\rho_0} \rho_0 2\pi = -1 \quad (2.41)$$

$$C_1 = -\frac{1}{4i} = \frac{i}{4} \quad (2.42)$$

2-D green function when the source is on origin is obtained after all these mathematical operations as indicated (2.43):

$$G(\rho) = \frac{i}{4} H_0^1(k\rho) \quad (2.43)$$

2-D green function when the source is not on origin is obtained with shifting. As seen equation (2.44):

$$G(\rho, \rho') = \frac{i}{4} H_0^1(k|\rho - \rho'|) \quad (2.44)$$

Importance of these equations are using the time variable $e^{-i\omega t}$. If $e^{i\omega t}$ is used for time variable, second order zero kind Henkel function with -1 coefficient is obtained cause of conjugation.

2.3 Discretization and Solution

Due to previous section, result of inhomogeneous differential equation with impulse response is obtained by green function properties as indicated from (2.45) to (2.46):

$$\nabla^2 G + k^2 G = -\delta(\vec{\rho} - \vec{\rho}') \quad (2.45)$$

$$G(\rho, \rho') = \frac{i}{4} H_0^1(k|\rho - \rho'|) \quad (2.46)$$

It is possible to solve scattering field equation with extend green function solution by convolution integral as indicated (2.47):

$$\nabla^2 u^s + k_0^2 u^s = -u \left(\frac{k^2}{k_0^2} - 1 \right) k_0^2 \quad (2.47)$$

The power rate between the wave number of background (in this formulation background) and scattering object is announced contras in literature and formulate as seen equation (2.48):

$$\chi(\rho') = \left(\frac{k^2}{k_0^2} - 1 \right) \quad (2.48)$$

Scattering field formulation on equation unknown, $u(\rho')$ this is called electric field on surface of object due to illumination by source. In this formulation ρ and ρ' are distances of source and observation point from origin. D is surface area of object and S is the space where object is lied on equation (2.49):

$$u^{\text{sct}}(\rho) = k_b^2 \int_D g(\rho - \rho') \chi(\rho') u(\rho') dv(\rho') \quad \rho \in S \quad (2.49)$$

Green function $g(\rho - \rho')$ is derivatived previous section and equation (2.50) obtained as :

$$u^{\text{sct}}(\rho) = k_b^2 \int_D \frac{i}{4} H_0^1(k|\rho - \rho'|) \chi(\rho') u(\rho') dv(\rho') \quad \rho \in S \quad (2.50)$$

Firstly, in order to calculate the total field, incident field is added both part of equation (2.50) and equation (2.51) is obtained as :

$$u^{\text{inc}}(\rho) + u^{\text{sct}}(\rho) = u^{\text{inc}}(\rho) + k_b^2 \int_D \frac{i}{4} H_0^1(k|\rho - \rho'|) \chi(\rho') u(\rho') dv(\rho') \quad \rho \in S \quad (2.51)$$

Next step integral equation is calculated on equation (2.52) while the source points are set to surface of object domain D.

$$u(\rho) = u^{\text{inc}}(\rho) + k_b^2 \int_D \frac{i}{4} H_0^1(k|\rho - \rho'|) \chi(\rho') u(\rho') dv(\rho') \quad \rho \in D \quad (2.52)$$

In order to solve complicated equation, method of moment's technique can be used to obtain linear equation system. Mom technique is based on discretization of integral equation with known functions as called basis function and unknown weighted residuals as indicated (2.53):

$$u = \sum_{n=1}^N u_n a_n ; \quad u_n = \text{unknown coefficient} , \quad a_n = \text{basis function} \quad (2.53)$$

In our problem, unit pulse function is selected as a basis function as indicated (2.54):

$$a_n = \begin{cases} 1 ; & \rho_m \\ 0 ; & \text{otherwise} \end{cases} \quad (2.54)$$

Scattering object surface is divided equal small surface area cells that field intensity is not changed on it and obtained equation as (2.55):

$$u_m = u_m^{\text{inc}} + k_b^2 \frac{i}{4} \sum_{n=1}^N \chi_n u_n \int_D H_0^1(k|\rho_m - \rho_n|) dv(\rho_n) \quad \rho \in D \quad (2.55)$$

It is possible to use delta Dirac instead of test function for simplicity. All these equations are written on matrix form as given equation (2.56):

$$[u^{\text{inc}}] = [u] [I - Z] \quad (2.56)$$

In this formulation, Z is called the surface impedance literature and u is called the indicated field on the surface of scattered object.

Scattered field outside of the object is calculated with numerically the integral equation as given equation (2.57). Integral solution can be found in [24].

$$u_m = k_b^2 \frac{i}{4} \sum_{m=1}^N u_m \int_D H_0^1(k|\rho_m - \rho_n|) dv(\rho_n) \quad \rho_m \in S \quad (2.57)$$



3. INVERSE PROBLEM

Inverse problems are concerned with determining causes for a desired or an observed effect. A practically important class of inverse problems is inverse scattering problems, where information about an unknown object (e.g., a body, an inhomogeneity in a material, a potential) is to be reconstructed from measurements or calculations by forward problem of waves or fields scattered by this object [25]. Inverse scattering problems are generally stated type of ill-posed problems. Given definition by Jacques Hadamard for well-posed problems must have solution, which is existence, unique and continuous dependence on the data. In most cases, uniqueness of inverse scattering problem is not provident due to scattering field data conditions. One of these conditions is impossibility the measurement or calculation of scattered field data for all incident direction. Even if it is possible, noise factor come into a play. The scattering field data is mostly obtained by numerical solution in case of exact solution due to construction of the problem. In addition, experimental (measurement) scattering field data always contains errors. For all these reasons small changes on exact value of scattering field data cause high difference from real value since the reconstruction of profile. Furthermore scattering field is nonlinear. Therefore, inverse scattering problems high nonlinearity causes ill-posed conditions. In spite of ill-posed conditions, inverse scattering problems are possibly solved by regularization methods.

3.1 Contrast Source Inversion Method

Contrast source inversion is a kind of minimization problem that reconstruct the contrast $\chi(\rho)$ with only knowledge of incident field u_j^{inc} and measured or synthetic scattered field data u_j^{sct} on possible existence domain. The contrast source inversion is type of quantitative method. Therefore, not only the shape but also electrical properties of scattered object can obtain by contrast source inversion method. Contrast source is also ill-posed and non-linear inverse scheme due to reasons as

indicated previous topic. Beside this contrast source inversion method does not require additional regularization since it converts the minimization problem into iterative quadratic programming problems.

In this thesis, the aim is to recover the stroke(s) in a brain from bistatic measurements taken at microwave frequency range. One of the canonical methods that can be utilized for this purpose is the contrast source inversion method. Then, at each distinct iteration the CSI method searches for the optimal direction and optimal update amount, which results in the minimal cost function value. By iterating on the problem up to a predefined threshold, the CSI method retrieves the arguments minimizing the cost functional, in other words the optimal values of the relative dielectric constant and conductivity of the brain.

Before going into detailed analysis, we have to define the basic assumptions of the problem in the hand. In this thesis, two-dimensional magnetic transverse (2D-TM) scattering problem case is assumed. More explicitly, the scattered (let us denote with Ω), which is a transverse slice of the head phantom (Zubal phantom), is assumed as infinite vertical direction. Furthermore, it is assumed that the head phantom is encovered and illuminated by a number of line sources (let us assume that the line sources are distributed on an arc Γ), which are also assumed as infinite vertical direction. Bistatic measurements are taken at several frequencies and obtained data is fed into the CSI method.

At the application stage of the CSI method, we will follow two different ways. First way, as in the canonical application of the CSI method, the head is measured once and the scattered field measurements are obtained by subtracting background signal from the former measurement. Here $u_{j,l}^s$ denotes the scattered field measured on Γ for j th incident field excitation at l th illumination frequency and $u_{j,l}^h, u_{j,l}^b$ stand for the simulated signal from the head phantom, background with same configuration. Second way, different from the canonical case, the head is measured twice and only the changes in the dielectric parameters are estimated from the difference of these two measurements. In a more explicit way, the scattered field measured on Γ for j th incident field excitation at l^{th} illumination frequency is computed as equation (3.1):

$$u_{j,l}^s = u_{j,l}^{h2} - u_{j,l}^{h1} \quad (3.1)$$

where $u_{j,l}^{h1}, u_{j,l}^{h2}$ are the simulated total electric fields arising from the head phantom in the first and second measurement, respectively.

Both kinds of measurements are supplied to the CSI algorithm. An important point to note is the data measured at different excitation frequencies are iteratively supplied to the CSI algorithm, i.e. the dielectric and conductivity distribution obtained at the output of the lower frequency step is utilized as the input of the next higher frequency. Such an iterative operation is remedy the inherent ill posedness CSI algorithm and make the obtained result more robust against noise and selection of the other system parameters.

3.2 Theoretical Background Contrast Source Inversion Method

As mentioned previous topic contrast source inversion method is aim to minimize the cost function as equation (3.2):

$$F(w_j, \chi) = \frac{\sum_j \|f_j - G_S w_j\|_S^2}{\sum_j \|f_j\|_S^2} + \frac{\sum_j \|\chi u_j^{inc} - w_j + \chi G_D w_j\|_D^2}{\sum_j \|\chi u_j^{inc}\|_D^2} \quad (3.2)$$

In equation 3.2 , the cost function linear combination of two normalize function. First term of the cost function, represent the error of the data equation where scattering field data u_j^{sct} represent f_j in the equation. This notation is preferred cause of compability previous studies in [26] about contrast source inversion methods. The second term of the cost function, represent the error of the object equation. u_j^{inc} terms indicates incident field and j indices indicates the angle of incident field. G_S is an operator mapping from $L^2(D)$ domain to $L^2(S)$ and defined equation as (3.3):

$$G_{S,D} \omega_j = \int_D \frac{i}{4} H_0^1(k|\rho - \rho'|) \chi(\rho') \omega(\rho') dv(\rho') \quad \rho \in \{S, D\} \quad (3.3)$$

Where contrast source ω_j is defined as equation (3.4):

$$\omega_j = \chi u_j \quad (3.4)$$

The contrast term χ as called object function is defined as equation (3.5):

$$\chi(r) = \frac{k^2}{k_b^2} - 1 \quad (3.5)$$

where k_b and k are the wavenumbers of background medium and scatterer respectively.

Purpose of contrast source inversion method is reconstruction the desired object from scattering filed data in order to minimize cost function. The cost function minimization is obtained by using update of contrast χ and contrast source w sequentially.

3.2.1 Contrast source updating steps

Following steps clarify the minimization of cost function. Firstly, object and data error is defined as equations (3.6) and (3.7):

$$\rho_{j,n} = f_{j,n} - G_S w_{j,n} \quad (3.6)$$

$$r_{j,n} = \chi_n u_{j,n}^{inc} - w_{j,n} \quad (3.7)$$

Where n indices is indicated the iteration number. Value of electrical field u_j is updated at iteration case as given equation (3.8):

$$u_{j,n} = u_j^{inc} + G_D w_{j,n} \quad (3.8)$$

Therefore, present value of contrast is required and obtained as given equation (3.9):

$$w_{j,n} = w_{j,n-1} + \alpha_{j,n}^w v_{j,n} \quad (3.9)$$

In this equation, $\alpha_{j,n}^w$ is a contrast parameter and $v_{j,n}$ is the Polak-Ribiere conjugate gradient direction. These are functions of positions. Initial values and iteration steps values of Polak-Ribiere conjugate direction is calculated as given equations (3.10) and (3.11):

$$v_{j,0} = 0, \quad (3.10)$$

$$v_{j,n} = g_{j,n}^w + \gamma_{j,n}^w v_{j,n-1}, \quad n \geq 1 \quad (3.11)$$

Where $g_{j,n}^w$ the Frechet derivative of the cost function with respect to $w_{j,n}$ is given in study [27] as equation (3.12):

$$g_{j,n}^w = \frac{\partial F_s(\omega_j)}{\partial(\omega_j)} = \left(\sum_j \|f_j\|_s^2 \right)^{-1} \lim_{\epsilon \rightarrow 0} \left(\frac{\|f_j - G_s(\omega_j + \epsilon g_j)\|_s^2 - \|f_j - G_s \omega_j\|_s^2}{\epsilon} \right) \quad (3.12)$$

$$\lim_{\epsilon \rightarrow 0} \left(\frac{(f_j^* - \omega_j^* G_s^* + \epsilon g_j G_s^*) (f_j - G_s \omega_j + G_s \epsilon g_j) - (f_j^* - \omega_j^* G_s^*) (f_j - G_s \omega_j)}{\epsilon} \right)$$

$$\lim_{\epsilon \rightarrow 0} \left(\frac{(f_j^* G_s \epsilon g_j - \omega_j^* G_s^* G_s \epsilon g_j + \epsilon g_j G_s^* f_j - \epsilon g_j G_s^* G_s \omega_j + \epsilon g_j G_s^* G_s \epsilon g_j)}{\epsilon} \right)$$

Nominator of the limit operation is displayed with dot product operator as given equation (3.13):

$$g_{j,n}^w = 2 \left(\sum_j \|f_j\|_s^2 \right)^{-1} \text{Re}\{\langle f_j^* - \omega_j^* G_s^*, G_s g_j \rangle\} \quad (3.13)$$

In equations (3.12) * is complex conjugate and transpose operator. Overbar on the contrast indicates complex conjugate operator.

The second part of the contrast function derivative is given as equation (3.14):

$$\frac{\partial F_d(\omega_j)}{\partial(\omega_j)} = \left(\sum_j \|\chi_{n-1} u_j^{inc}\|_d^2 \right)^{-1} \lim_{\epsilon \rightarrow 0} \left(\frac{\|\chi u_j^{inc} - (w_j + \epsilon) + \chi G_d(w_j + \epsilon)\|_d^2 - \|\chi u_j^{inc} - w_j + \chi G_d w_j\|_d^2}{\epsilon} \right) \quad (3.14)$$

In this study normalize values of denominators notations are (3.15) and (3.16):

$$\eta_s = \left(\sum_j \|f_j\|_s^2 \right)^{-1} \quad (3.15)$$

$$\eta_{D,n-1} = \left(\sum_j \|\chi u_j^{inc}\|_D^2 \right)^{-1} \quad (3.16)$$

Also norm operation is carried out with inner product given as equation (3.17):

$$\eta_D = \langle A^*, A \rangle_D \quad (3.17)$$

Gradient of the cost function is obtained due to results of equations (3.12) and (3.14) and indicated (3.18):

$$g_{j,n}^w = -\frac{G_S^* \rho_{j,n-1}}{\sum_j \|f_j\|_S^2} - \frac{r_{j,n-1} - G_D^* (\bar{\chi}_{n-1} r_{j,n-1})}{\sum_j \|\chi_{n-1} u_j^{inc}\|_D^2} \quad (3.18)$$

The parameter $\gamma_{j,n}^\omega$ determines the difference of previous and present gradients. In van der berg [26-27] study this parameter is given equations (3.19):

$$\gamma_{j,n}^w = \frac{Re \langle g_{j,n}^w, g_{j,n}^w - g_{j,n-1}^w \rangle_D}{\langle g_{j,n-1}^w, g_{j,n-1}^w \rangle_D} \quad (3.19)$$

In our study, Polak-Ribiere conjugate gradient with given $\gamma_{j,n}^w$ parameter makes trouble. In each iteration steps minimization of cost function is not obtained. In order to prevent this situation $\gamma_{j,n}^w$ is changed with its single-frequency approach value as given equations (3.20):

$$\gamma_n^w = \frac{Re \sum_j \langle g_{j,n}^w, g_{j,n}^w - g_{j,n-1}^w \rangle_D}{\sum_j \langle g_{j,n-1}^w, g_{j,n-1}^w \rangle_D} \quad (3.20)$$

Update algorithm completes within determining the constant parameter $\alpha_{j,n}^w$ at the update equation (3.9). The contrast source term w_j at the cost function is replaced with equation includes its previous values and Polak-Ribiere on cost function iterative values as equations (3.21):

$$\begin{aligned}
& F_n(w_{j,n-1} + \alpha_{j,n}^w v_{j,n}, \chi_n) \\
&= \frac{\sum_j \|f_j - G_S(w_{j,n-1} + \alpha_{j,n}^w v_{j,n})\|_S^2}{\sum_j \|f_j\|_S^2} \\
&+ \frac{\sum_j \|\chi u_j^{inc} - (w_{j,n-1} + \alpha_{j,n}^w v_{j,n}) + \chi G_D(w_{j,n-1} + \alpha_{j,n}^w v_{j,n})\|_D^2}{\sum_j \|\chi u_j^{inc}\|_D^2}
\end{aligned} \tag{3.21}$$

The constant parameter $\alpha_{j,n}^w$ is determined with given cost function minimization.

After mathematical operation $\alpha_{j,n}^w$ obtained given as indicated (3.22):

$$\alpha_{j,n}^w = \frac{-\langle g_{j,n}, v_{j,n} \rangle_D}{\eta_S \sum_j \|G_S v_{j,n}\|_S^2 + \eta_{D,n-1} \sum_j \|v_{j,n} - \chi_{n-1} G_D v_{j,n}\|_D^2} \tag{3.22}$$

In our study, the constant parameter $\alpha_{j,n}^w$ is changed with its single-frequency approach value due to same reasons as indicated $\gamma_{j,n}^w$ determination and given as indicated (3.23):

$$\alpha_n^w = \frac{-Re \sum_j \langle g_{j,n}, v_{j,n} \rangle_D}{\eta_S \sum_j \|G_S v_{j,n}\|_S^2 + \eta_{D,n-1} \sum_j \|v_{j,n} - \chi_{n-1} G_D v_{j,n}\|_D^2} \tag{3.23}$$

3.2.2 Contrast updating steps

Second main step of contrast source inversion method is minimization the cost function due to contrast term χ . Only the right hand side of the cost function that is announced object equation, includes contrast term. Minimization of object equation is obtained by two ways. First way is updating the contrast term in order to minimize the nominator of the object equation by the present value of contrast source by some mathematical operations. Contrast source is product of unknown field inside the scattered object and the contrast as defined previously as indicated (3.24):

$$w_{j,n}(r') = \chi_n(r') u_{j,n}(r') \tag{3.24}$$

The contrast source equations both side product with conjugate of field as shown equations from (3.25) to (3.27):

$$w_{j,n}(r')\overline{u_{j,n}}(r') = \chi_n(r')u_{j,n}(r')\overline{u_{j,n}}(r') \quad (3.25)$$

$$w_{j,n}(r')\overline{u_{j,n}}(r') = \chi_n(r')\cdot |u_{j,n}(r')|^2 \quad (3.26)$$

$$\chi_n = \frac{\sum_{j=1} \omega_{j,n} (\overline{u_{j,n}})}{\sum_j |u_{j,n}|^2} \quad (3.27)$$

Second way is updating the contrast term by nonlinear conjugate gradient scheme. The nonlinear conjugate gradient method is generally used to find the local minimum of a nonlinear function using its gradient. As mentioned before conjugate gradient is iterative method, since χ_{n-1} is known, present value of contrast χ is found as given equations (3.28):

$$\chi_n = \chi_{n-1} + \alpha_n^\chi d_n \quad (3.28)$$

In this formula, α_n^χ is a constant parameter that is and d_n is the steepest direction to local minima. Updating the conjugate direction is determined as given equations (3.29):

$$d_n = g_n^\chi + \gamma_n^\chi d_{n-1} \quad (3.29)$$

The parameter γ_n^χ is calculated based on gradient of our nonlinear cost function due to contrast with Polak-Ribiere formulation as given below equations (3.30):

$$\gamma_n^\chi = \frac{Re \sum_j \langle g_{j,n}^\chi, g_{j,n}^\chi - g_{j,n-1}^\chi \rangle_D}{\langle g_{j,n-1}^\chi, g_{j,n-1}^\chi \rangle_D} \quad (3.30)$$

Gradient $g_{j,n}^\chi$ is determined with neglecting the changes the contrast in denominator of second part of contrast source is calculated as equations (3.31) and obtained (3.32):

$$\frac{\partial F_D(\chi_j)}{\partial(\chi_j)} = g_{j,n}^\chi = \left(\sum_j \|\chi_{n-1} u_j^{inc}\|_D^2 \right)^{-1} \quad (3.31)$$

$$\lim_{\epsilon \rightarrow 0} \left(\frac{\|(\chi + \epsilon g_{j,n}^\chi) u_j^{inc} - w_j + (\chi + \epsilon g_{j,n}^\chi) G_D w_j\|_D^2 - \|\chi u_j^{inc} - w_j + \chi G_D w_j\|_D^2}{\epsilon} \right)$$

$$g_{j,n}^\chi = \frac{\sum_{j=1} (\chi_{n-1} u_{j,n} - \omega_{j,n}) \overline{u_{j,n}}}{\sum_j \|\chi_{n-1} u_j^{inc}\|_D^2} \quad (3.32)$$

To improve convergence speed preconditioned conjugate gradient method that is given in (3.33) is used in order to equation (3.32):

$$g_{j,n}^\chi = \frac{\sum_{j=1} (\chi_{n-1} u_{j,n} - \omega_{j,n}) \overline{u_{j,n}}}{\sum_j \|u_{j,n}\|^2 \sum_j \|\chi_{n-1} u_j^{inc}\|_D^2} \quad (3.33)$$

The constant parameter α_n^χ is found by minimization of cost function as given formula (3.34):

$$F_n(\chi_{n-1} + \alpha_n^\chi d_n) = \frac{\sum_j \|(\chi_{n-1} + \alpha_n^\chi d_n) u_{j,n} - \omega_{j,n}\|_D^2}{\sum_j \|(\chi_{n-1} + \alpha_n^\chi d_n) u_j^{inc}\|_D^2} \quad (3.34)$$

$$\frac{a(\alpha_n^\chi)^2 + 2b\alpha_n^\chi + c}{A(\alpha_n^\chi)^2 + 2B\alpha_n^\chi + C} \quad (3.35)$$

The coefficients on the equations (3.35) are defined in van der berg study [27] as equations from (3.36) to (3.41):

$$a = \sum_j \|d_n u_{j,n}\|_D^2 \quad (3.36)$$

$$A = \sum_j \|d_n u_j^{inc}\|_D^2 \quad (3.37)$$

$$b = \text{Re} \sum_j \langle \chi_{n-1} u_{j,n} - w_{j,n}, d_n u_{j,n} \rangle_D \quad (3.38)$$

$$B = \text{Re} \sum_j \langle \chi_{n-1} u_j^{\text{inc}}, d_n u_j^{\text{inc}} \rangle_D \quad (3.39)$$

$$c = \sum_j \| \chi_{n-1} u_{j,n} - w_{j,n} \|_D^2 \quad (3.40)$$

$$C = \sum_j \| \chi_{n-1} u_j^{\text{inc}} \|_D^2 \quad (3.41)$$

The minimization equation (3.34) is ratio of two quadratic functions and the constant parameter α_n^x is defined with these two quadratic functions numerical coefficients as given (3.42):

$$\alpha_n^x = \frac{-(aC - Ac) + \sqrt{(aC - Ac)^2 - 4(aB - Ab)(bC - Bc)}}{2(aB - Ab)} \quad (3.42)$$

3.2.3 Initial values of contrast source inversion method

Zero initial values for contrast and contrast source term make undefined the cost function. For this reason, we estimate the starting values of contrast source to minimize data error as given formula (3.43):

$$F_s(\alpha_0^\omega) = \frac{\sum_j \|f_j - G_s \alpha_0^\omega g_{j,0}^\omega\|_s^2}{\sum_j \|f_j\|_s^2} \quad (3.43)$$

To find the minimum of cost function we derivate it α_0^ω variable and it is value to zero as calculated in equations (3.44) and find (3.45):

$$\frac{dF_s}{d\alpha_0^\omega} = \frac{d}{d\alpha_0^\omega} \left(\frac{\sum_j (f_j - G_s \alpha_0^\omega g_{j,0}^\omega)^* (f_j - G_s \alpha_0^\omega g_{j,0}^\omega)}{\sum_j \|f_j\|_s^2} \right) \quad (3.44)$$

$$\frac{d}{d\alpha_0^\omega} \left(\frac{\sum_j (f_j f_j^* - G_S^* \alpha_0^\omega g_{j,0}^\omega f_j - \alpha_0^\omega G_S g_{j,0}^\omega f_j^* + \alpha_0^{\omega^2} G_S^* g_{j,0}^\omega G_S g_{j,0}^\omega)}{\sum_j \|f_j\|_S^2} \right) = 0$$

$$\frac{\sum_j (G_S^* g_{j,0}^\omega f_j - G_S g_{j,0}^\omega f_j^* + 2\alpha_0^\omega G_S^* g_{j,0}^\omega G_S g_{j,0}^\omega)}{\sum_j \|f_j\|_S^2} = 0$$

$$\alpha_0^\omega = \frac{\sum_j (G_S^* g_{j,0}^\omega f_j + G_S g_{j,0}^\omega f_j^*)}{2 \sum_j \|G_S g_{j,0}^\omega\|_S^2} \quad (3.45)$$

Nominator of the limit operation is displayed with dot product operator as given equations (3.46):

$$\alpha_0^\omega = \frac{2 \operatorname{Re}\{\sum_j (G_S g_{j,0}^\omega f_j^*)\}}{2 \sum_j \|G_S g_{j,0}^\omega\|_S^2} = \frac{\sum_j \langle f_j, G_S g_{j,0}^\omega \rangle_S^2}{\sum_j \|G_S g_{j,0}^\omega\|_S^2} \quad (3.46)$$

For determining constant parameter, α_0^ω initial value of gradient is required.. The gradient $g_{j,0}^\omega$ is found by take the value of previous contrast source term from initial time zero with gradient of cost function and obtained as given equation (3.47):

$$\omega_{j,0} = \alpha_0^\omega g_{j,0}^\omega, \quad g_{j,0}^\omega = G_S^* f_j \quad (3.47)$$

Where $g_{j,0}^\omega$ is called a backpropagation of the field data. Initial value of contrast term and filed can be determined with using initial values of contrast source in equations (3.48) and (3.49):

$$\chi_0 = \frac{\sum_{j=1} \omega_{j,0} (\overline{u_{j,0}})}{\sum_j |u_{j,0}|^2} \quad (3.48)$$

$$u_{j,0} = u_j^{\text{inc}} + G_D w_{j,0} \quad (3.49)$$



4. NUMERICAL RESULTS

4.1 Simulation Setup

In this thesis, a realistic 3D head phantom model, which is result of study [28], is used. The head phantom ingenerates 128 transverse MRI images, which are taken from 3D head model. In each slice, tissues are represented with 256 x 256dimension matrix which contains 62 index numbers. Index numbers are variance due to tissue's anatomical, neurological and taxonomical properties. Although these are many different types' tissues, only seven are used for reduce difficulties of problem. The used tissues are skin, skull, fat, dura, cerebral spinal fluid (CSF), gray matter, white matter. The index numbers are mapped to the dielectric permittivity and conductivity of related tissues in the head. The dielectric constant and conductivity as a function of frequency are determined by second order Debye model presentation in study [29]. The 2nd order Debye model and parameters are given by equation (4.1) and Table 4.1, respectively [29].

$$\epsilon_d(\omega) = \epsilon_\infty + (\epsilon_s - \epsilon_m)/(1 + j\omega\tau_1) + \frac{\epsilon_m - \epsilon_\infty}{1 + j\omega\tau_2} + \frac{\sigma}{j\omega\epsilon_0} \quad (4.1)$$

where ϵ_d , ϵ_∞ and ϵ_s are Debye fitting parameters, ω is the angular frequency while $\tau_{1,2}$ are time constant, ϵ_0 is the permittivity of free space .

Table 4.1 : 2nd Order Debye parameters for different types tissues

Tissue	ϵ_s	ϵ_m	ϵ_∞	$\tau_1(pS)$	$\tau_2(pS)$	$\sigma(S/m)$
Skin	192	38	4	1856	9.5	0.0002
Skull	20	11	2.5	961	15	0.02
Fat	5	0.7	2.5	13	13	0.01
CSF	102	67	4	1212	9.1	2
Dura	118	43	4	2042	10.2	0.5
Grey Matter	237	50	4	2269	10.8	0.02
White Matter	129	37	4	1850	10.8	0.02
Blood	306	60	4	3471	10.3	0.7

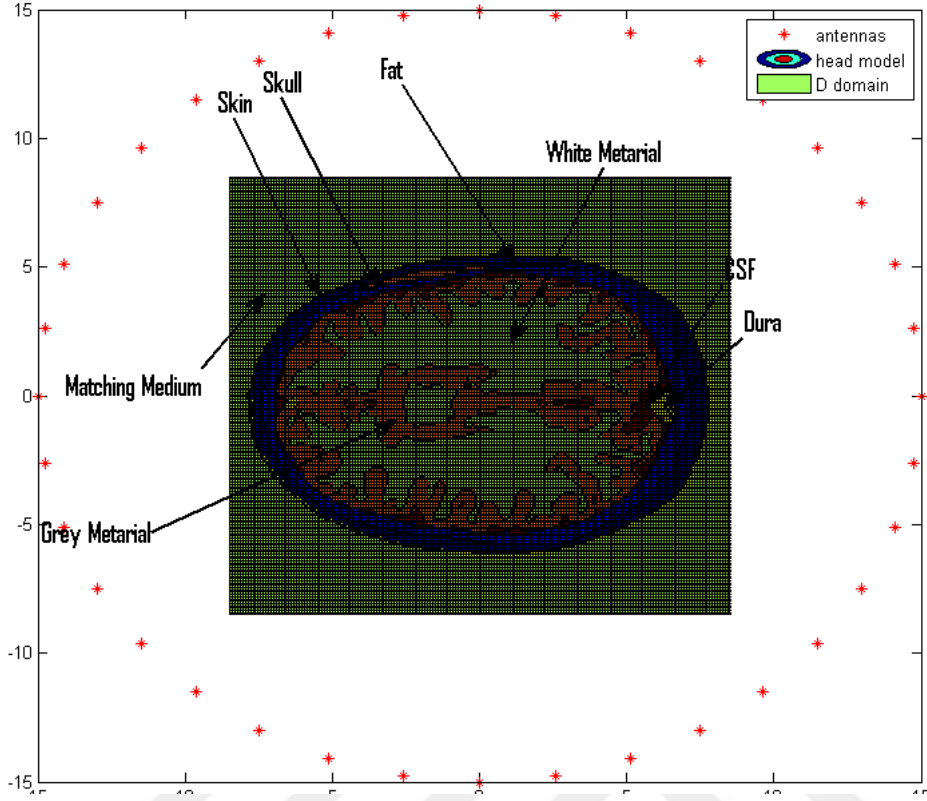


Figure 4.1: Measurement system configuration.

A numerical system shown in Figure 4.1 is set up in Matlab platform. A slice, which is 48 ordered from the Zubal Phantom, is taken. Blood region of various size are added at different location on the head model for different scenarios. The head model is assumed to be inside a square shape domain D which dimensions are 1.7cm x 1.7cm. The outside region is assumed to be filled by a matching medium with various dielectric constants for various scenarios. Matching medium decreases the contrast between the electromagnetic parameters of the outside the region, and those of the human head. The domain is illuminated by 36 TM line sources as given :

$$u(r, r') = \frac{i}{4} H_0^1(k|r - r'|) \quad (4.2)$$

where located on a circle with a radius of 17cm as depicted in Figure 4.2 for all applications. The operation frequency is chosen from 500MHz to 1.2GHz for various scenarios. The lower frequencies are not chosen due to require unreal antenna sizes. Furthermore, higher than 1.2 GHz frequencies are not chosen due to low penetration

electromagnetic fields into the head model. Scattering field is calculated numerically by a method of moments as mentioned on section 2. For the solution of direct scattering problem, the domain is divided into 196×196 cells. To prevent inverse crime different meshing of 65×65 cells is used for the inverse problem. For realistic scenarios, minimum $SNR = 30dB$ white additive Gaussian noise is added to scattering fields' data.

4.2 Results of Contrast Source Algorithm (Positive Constraint)

In order to test the performance of the proposed method, Zubal phantom model with blood region is reconstructed at different operating frequency. For all these simulations under this topic, a matching medium is used with a dielectric parameters $\epsilon_r = 20$ and $\sigma = 0 S/m$. The rebuilt zubal head model that contains the dielectric properties of tissues is set up in matlab simulation platform. The square shape blood region that is shown with red colour in Figure 4.2, is assumed to be centered at the point $x=1cm$, $y=2.2cm$, and has the dimensions of $2.6 cm \times 2.6 cm$. Blood region is shown with light yellow colour in Figure 4.3 due to low conductivity than CSF. Skin and skull that is the head model tissues near the outside region, appearance clearly in Figure 4.4.

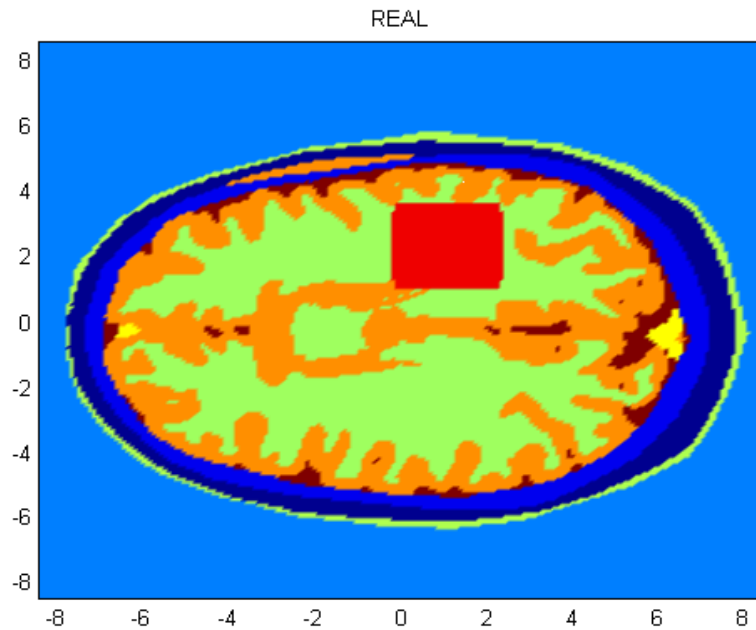


Figure 4.2 : Electrical properties of head phantom (real part of contrast)

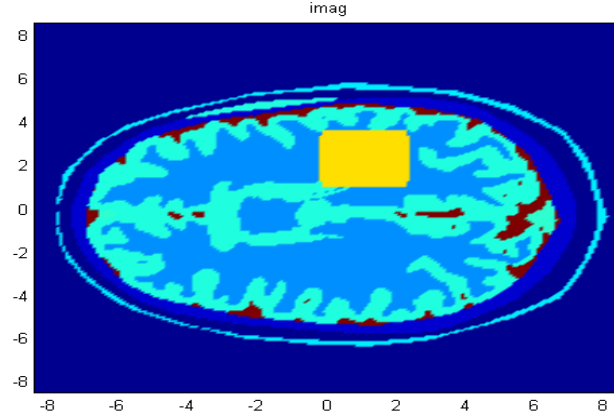


Figure 4.3 : Electrical properties of head phantom (imaginary part of contrast)

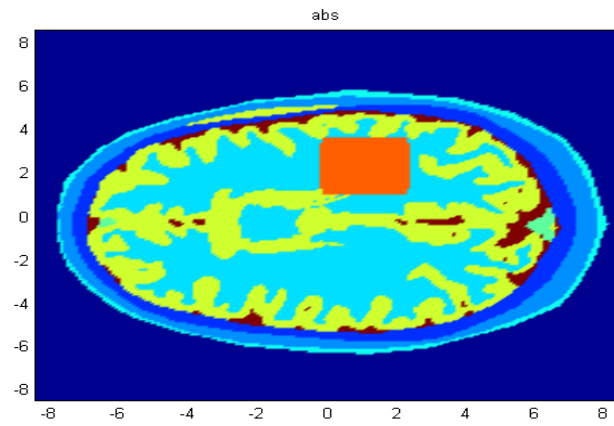


Figure 4.4 : Electrical properties of head phantom (absolute value of contrast)

After reconstruction from scattering field data by CSI method at 500MHz frequency, blooded area is shown with dark red colour in Figure 4.5. Blood region is centered approximately at the point $x=1\text{cm}$, $y=1.7\text{cm}$. Blood region size is larger than its owner size and location of blood region cannot be determined significantly due to low resolution at these frequencies. Imaginary value of contrast that is shown in Figure 4.6, does not present clear information about blooded area due to being dominant of CSF with higher conductivity. The skin and skull are more distinct on absolute contrast value in Figure 4.7 of head phantom.

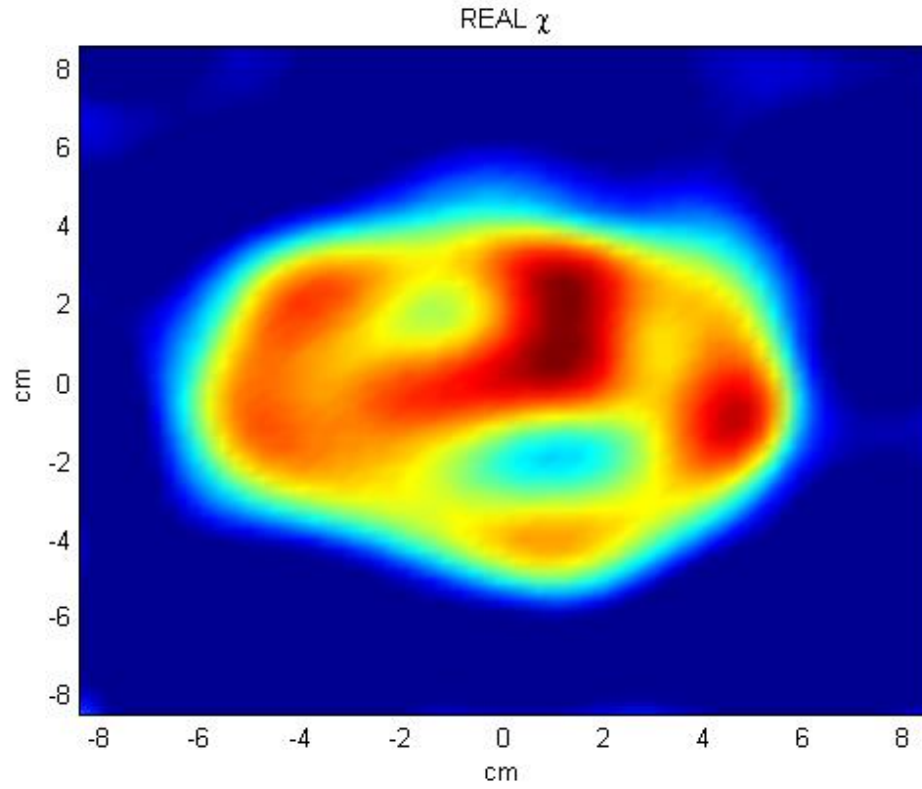


Figure 4.5 : Real part of contrast on Microwave imaged by CSI algorithm of the phantom with 500Mhz operation frequency

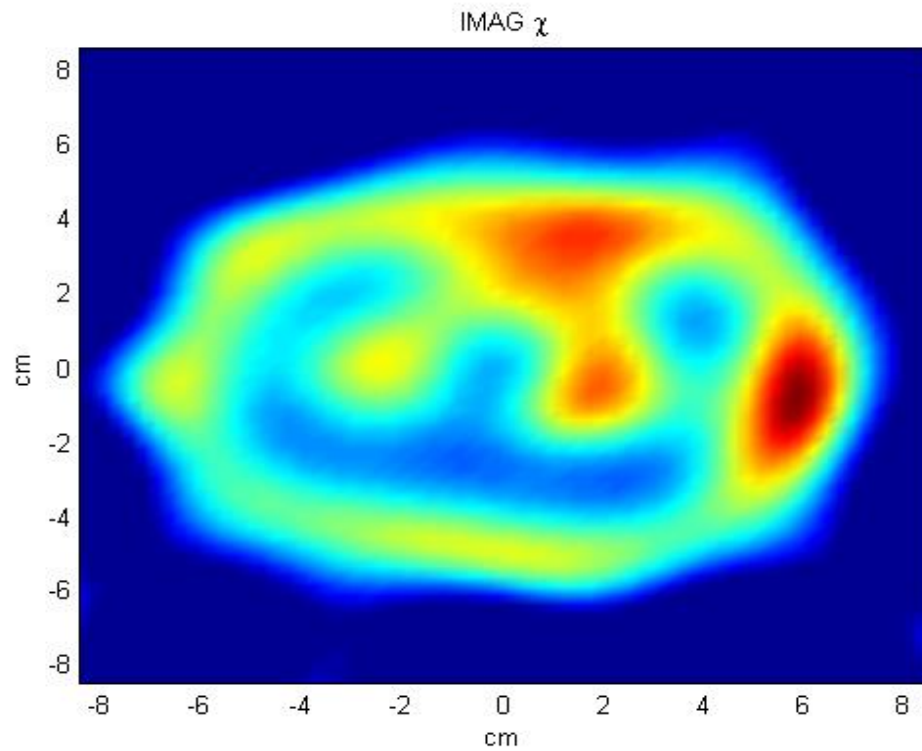


Figure 4.6 : Imaginary part of contrast on Microwave imaged by CSI algorithm of the phantom with 500Mhz operation frequency

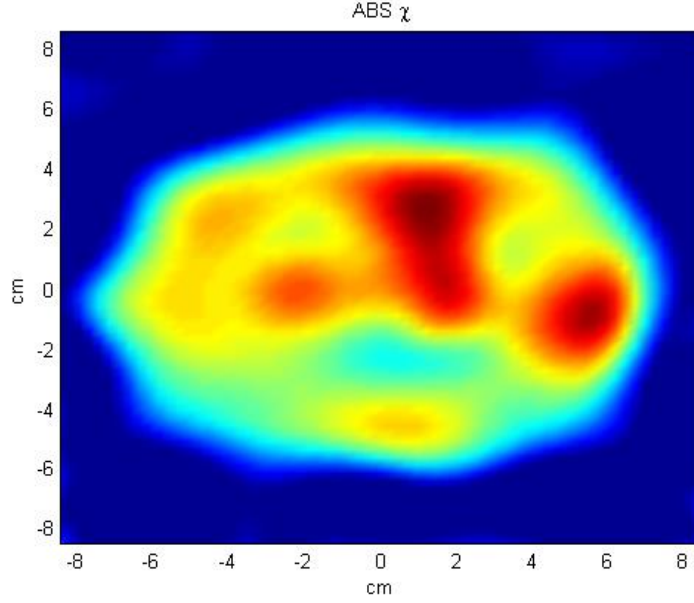


Figure 4.7 : Absolute value of contrast on Microwave imaged by CSI algorithm of the phantom with 500Mhz operation frequency

When the operation frequency is increased to 800 MHz, the quality of the result is increased as seen in Figure 4.8. Here, the reconstructed blood region is centered at $x=0.9\text{cm}$, $y=1.96\text{cm}$. Blood region cannot be detected on imaginary value of contrast that is shown in Figure 4.9 while CSF is clearly detectable. The blood region and the shape of head is more distinct on absolute contrast value in Figure 4.10.

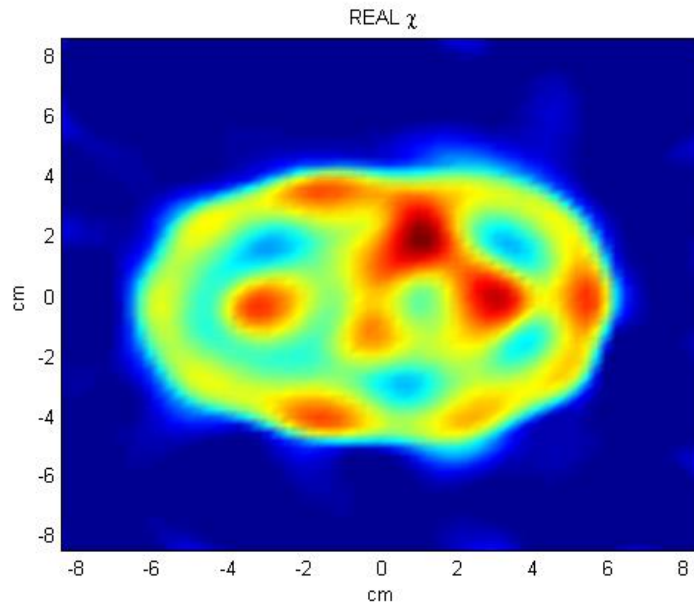


Figure 4.8 : Real part of contrast on Microwave imaged by CSI algorithm of the phantom with 800Mhz operation frequency

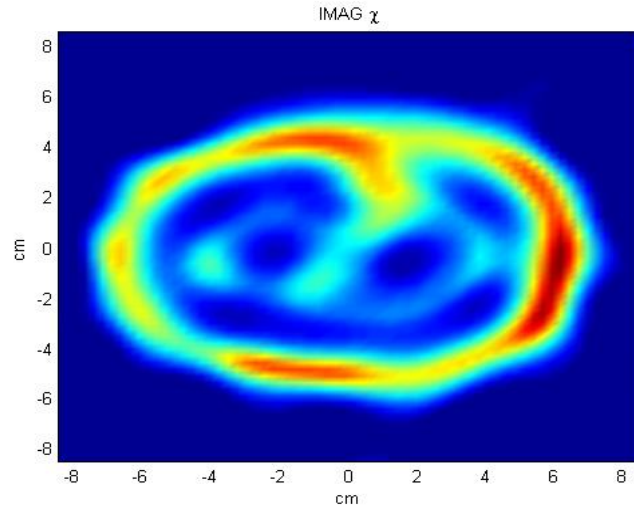


Figure 4.9 : Imaginary part of contrast on Microwave imaged by CSI algorithm of the phantom with 800Mhz operation frequency

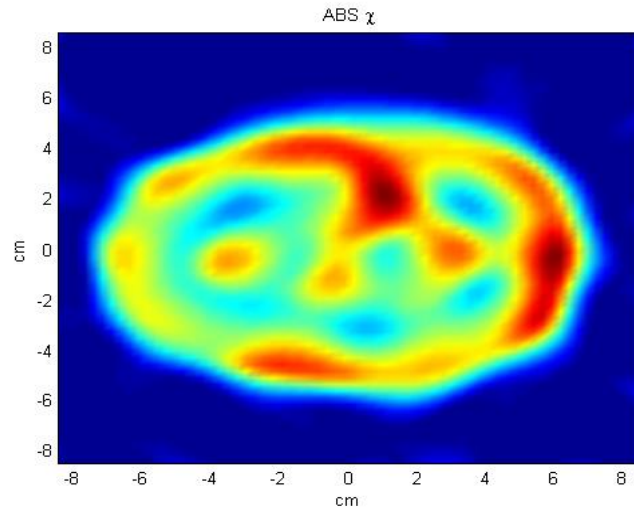


Figure 4.10 : Absolute value of contrast on Microwave imaged by CSI algorithm of the phantom with 800Mhz operation frequency

The reconstructions with 1GHz operating frequencies are presented in Figures 4.11-4.13. As shown in Figure 4.11 the blood area center shifts to point $x=0.65\text{cm}$, $y=1.7\text{cm}$. In addition, other regions of the brain, namely CSF, start to be more dominant, and to affect the quality of the results. It is clear from these examples that the imaginary parts of the contrast as shown in Figure 4.12 do not provide meaningful results, probably because of the high value of CSF conductivity. Since shape of brain reconstruction is more succeeding at 1Ghz frequency on absolute value of contrast as shown in Figure 4.13.

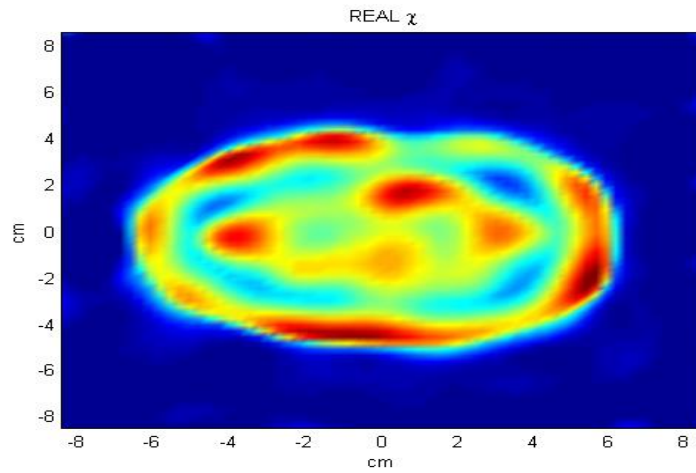


Figure 4.11 : Real part of contrast on Microwave imaged by CSI algorithm of the phantom with 1GHz operation frequency

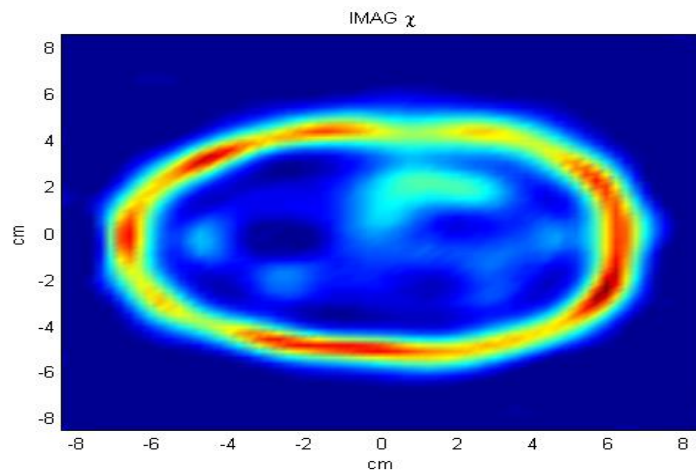


Figure 4.12 : Imaginary part of contrast on Microwave imaged by CSI algorithm of the phantom with 1GHz operation frequency

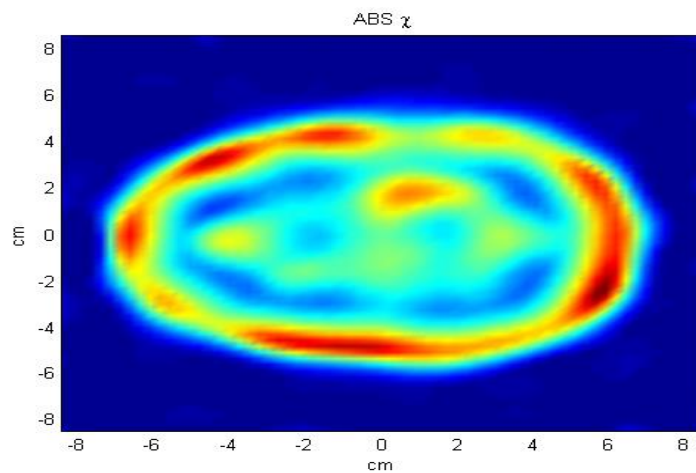


Figure 4.13 : Absolute value of contrast on Microwave imaged by CSI algorithm of the phantom with 1GHz operation frequency

Detection of blooded region becomes impossible at 1.2GHz and higher frequencies as shown in Figure 4.14-4.16. Furthermore, neither real value as shown in Figure 4.14 nor imaginary and absolute value of contrast Figure 4.15-4.16 gives information about shape or any other tissues expect skin and skull.

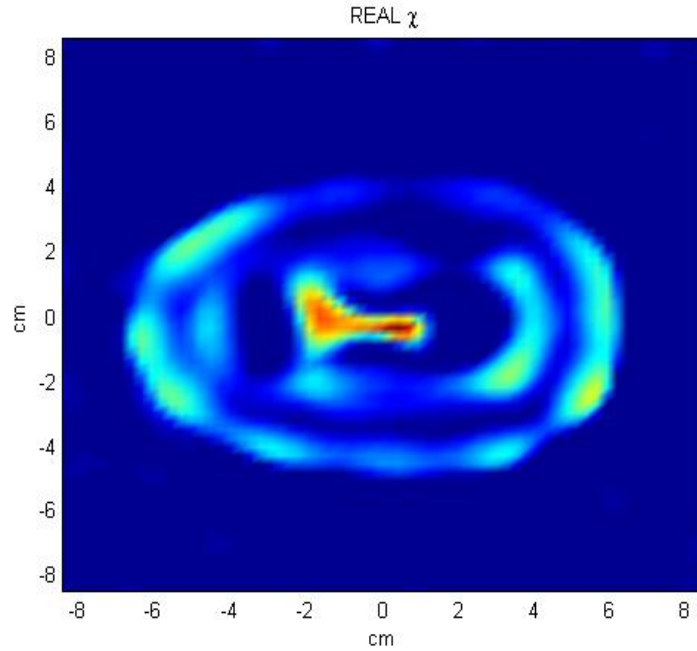


Figure 4.14 : Real part of contrast on Microwave imaged by CSI algorithm of the phantom with 1.2GHz operation frequency

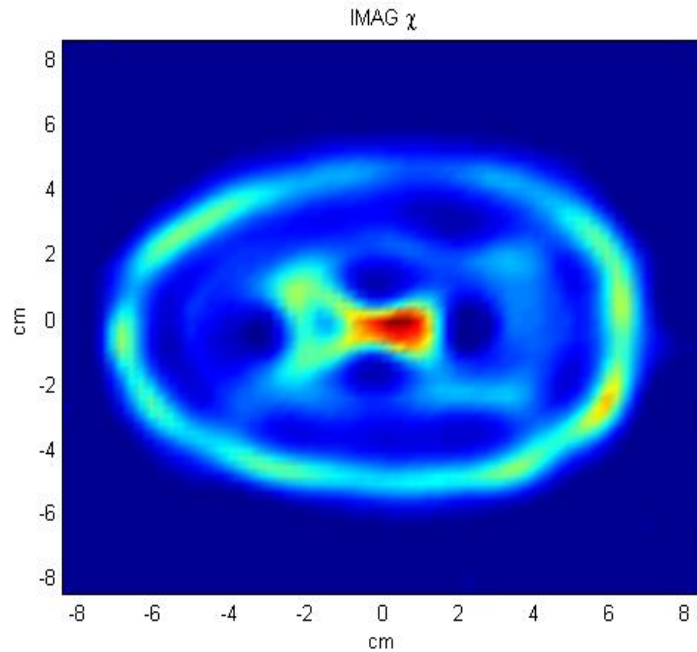


Figure 4.15 : Imaginary part of contrast on Microwave imaged by CSI algorithm of the phantom with 1.2GHz operation frequency

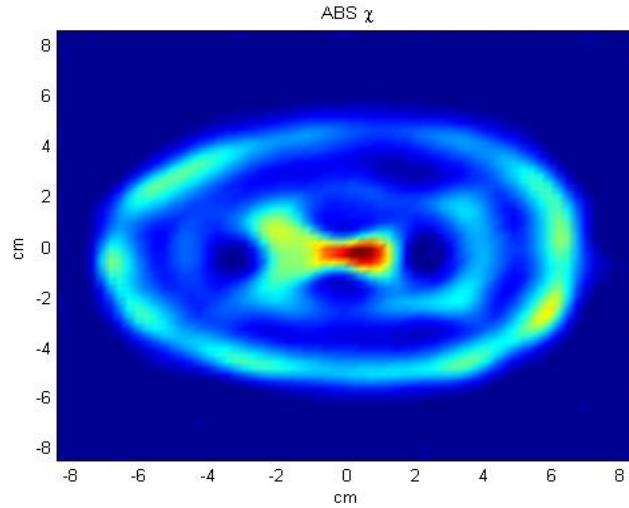


Figure 4.16 : Absolute of contrast on Microwave imaged by CSI algorithm of the phantom with 1.2GHz operation frequency

Location of blooded region on head model is importance of microwave imaging. To examine the location effects on results, a blood region at the central part of the brain is investigated as shown in Figure 4.17 example. For this simulation, the center of the blood region is determined as $x=-0.6\text{cm}$, $y=-0.3\text{cm}$, nearly the center of the investigation domain. The operating frequency is chosen as $f=1\text{GHz}$. The reconstructions given in Figure 4.18-4.20 demonstrate that the method is capable of locating blood regions in the inner parts of the human brain. However, it should be noted here that, the size of the blood region is of critical importance. The CSI based method is sufficient for detecting the various location of blooded area.

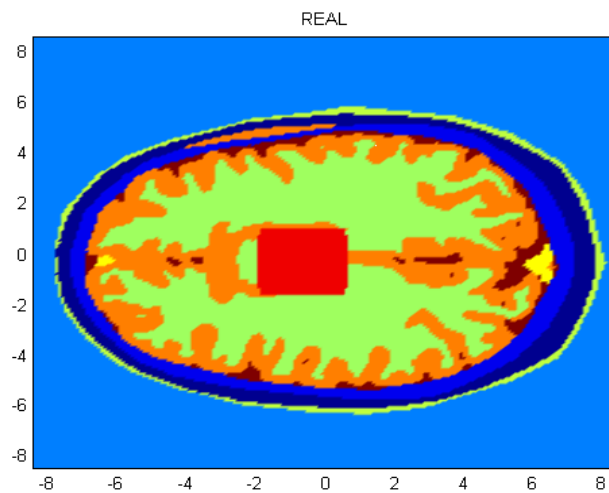


Figure 4.17 : Electrical properties of head phantom with different centered blooded area (real value of contrast)

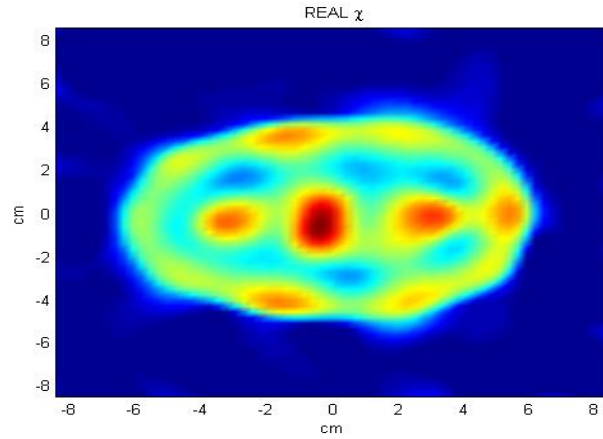


Figure 4.18 : Real part of contrast on Microwave imaged by CSI algorithm of the phantom with 1GHz operation frequency

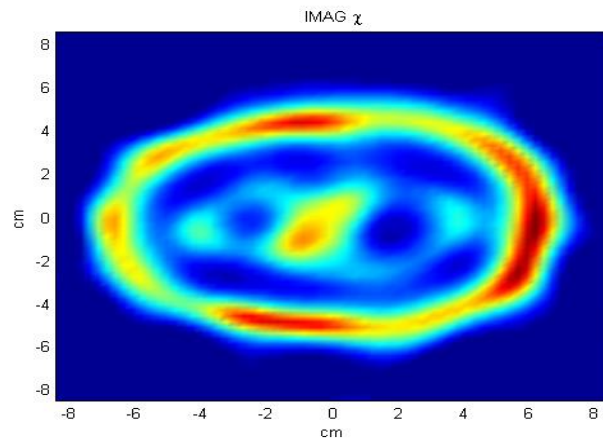


Figure 4.19 : Imaginary part of contrast on Microwave imaged by CSI algorithm of the phantom with 1GHz operation frequency

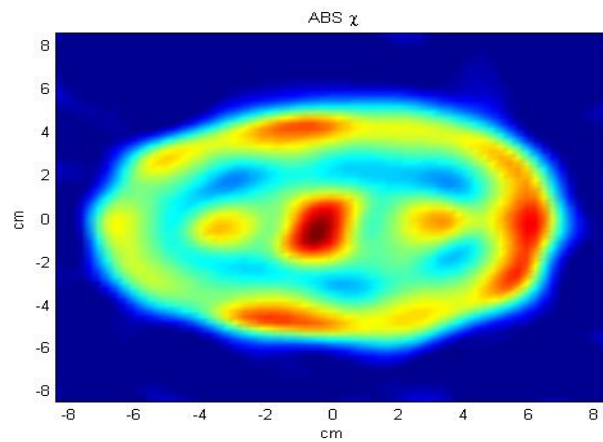


Figure 4.20 : Absolute value of contrast on Microwave imaged by CSI algorithm of the phantom with 1GHz operation frequency

To determine the effects of matching medium, the head model without matching medium as shown in Figure 4.21 is reconstructed. Reconstructed images in Figure 4.22-4.24 do not give any information about the blood neither it's location nor it's shape. High contrast difference between the air and head model cause difficulties of electromagnetic waves penetration into the head model.

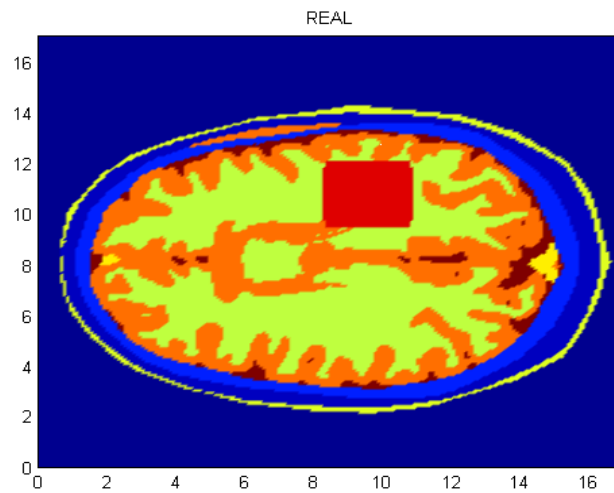


Figure 4.21 : Electrical properties of head phantom without matching medium (real value of contrast)

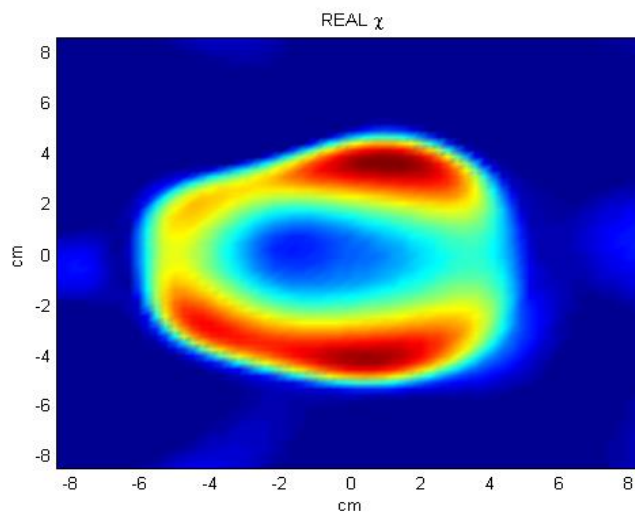


Figure 4.22 : Real part of contrast on Microwave imaged by CSI algorithm of the phantom with 500MHz operation frequency and without matching medium

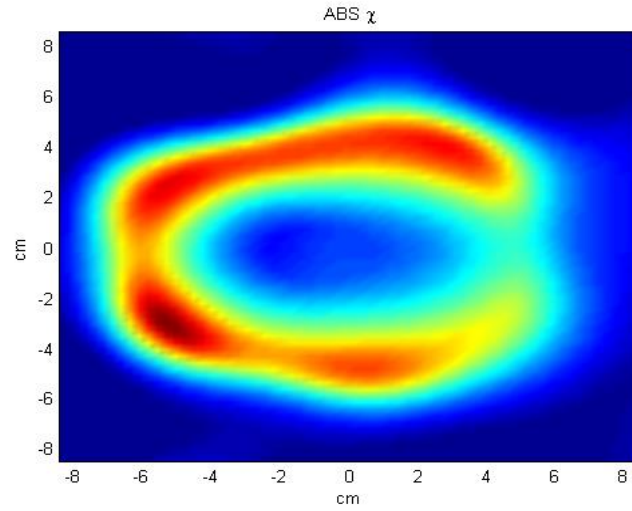


Figure 4.23 : Absolute value of contrast on Microwave imaged by CSI algorithm of the phantom with 500MHz operation frequency and without matching medium

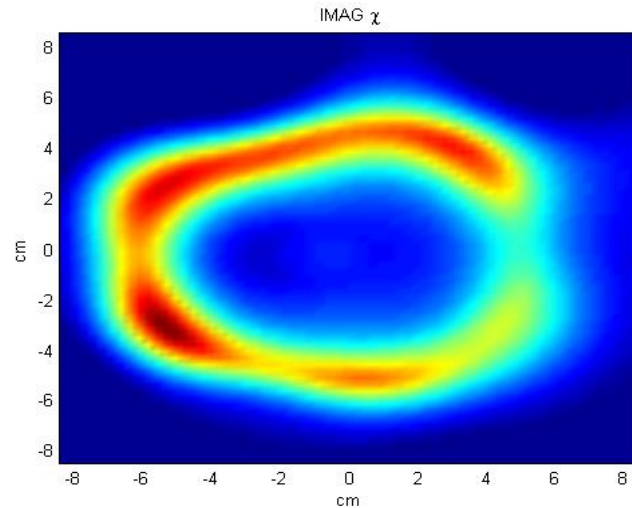


Figure 4.24 : Imaginary part of contrast on Microwave imaged by CSI algorithm of the phantom with 500MHz operation frequency and without matching medium

4.3 Results of Contrast Source Algorithm (No Positive Constraint)

Since using the method with positive constraint is not physically true, it provides the results of microwave imaging comparing the without using this approach. However, using positive constraint improves the detection of blooded region; shape of head is not reconstructed truly due to negative contrast of the head model parts especially near the outside area like skin, skull, and fat. Hence, microwave imaging of the head

model is realized with CSI method and without any constraint. The square shape blood region that is shown with large yellow colour in Figure 4.25, is assumed to be centered at the point $x=10.9\text{cm}$, $y=11.7\text{cm}$, and has the dimensions of $2.6\text{ cm} \times 2.6\text{ cm}$ same as used previous section.

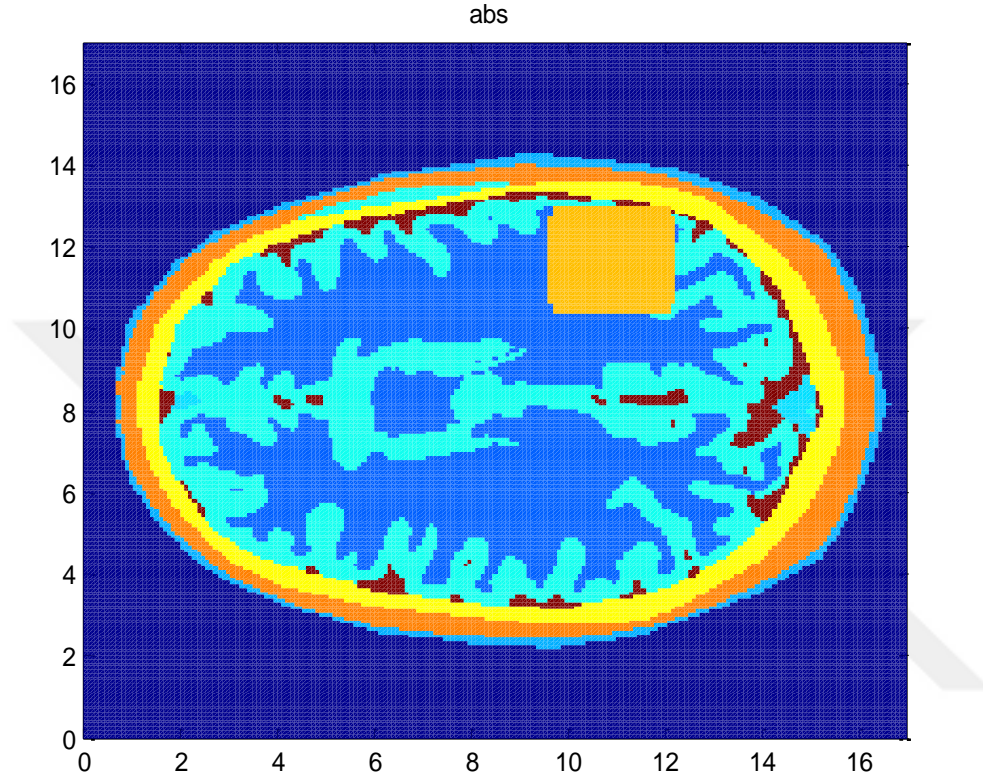


Figure 4.25 : Electrical properties of head phantom with matching medium (real value of contrast)

After reconstruction from scattering field data by CSI method without any constraint and with using matching medium that's dielectric contrast is $\epsilon_b=20$ at 500MHz frequency, blooded area is shown with dark red colour in Figure 4.26. Blood region darkest area is centered approximately at the point $x = 11.2\text{cm}$, $y=11.2\text{cm}$. Blood region is detected although it attempts to area where CSF is highly located on reconstructed in Figure 4.26. Imaginary and absolute values of contrast gives explicit results about the location of blood region that is centered approximately at the point $x = 10.9\text{cm}$, $y=12.3\text{cm}$ in Figure 4.27-4.28.

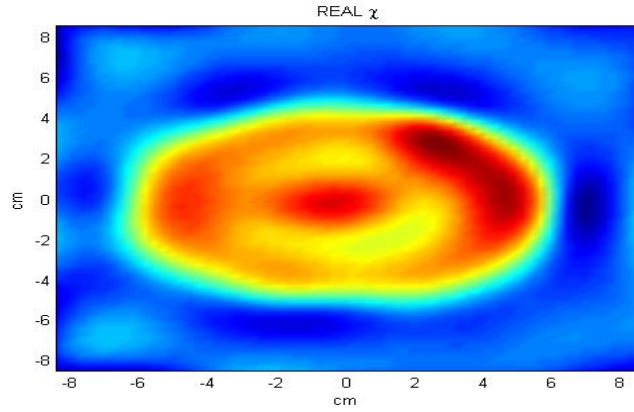


Figure 4.26 : Real part of contrast on Microwave imaged by CSI algorithm of the phantom with 500MHz operation frequency and with matching medium $\epsilon_b = 20$

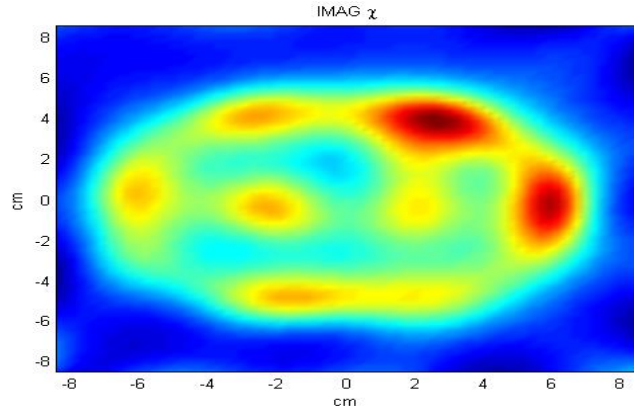


Figure 4.27 : Imaginary part of contrast on Microwave imaged by CSI algorithm of the phantom with 500MHz operation frequency and with matching medium $\epsilon_b = 20$

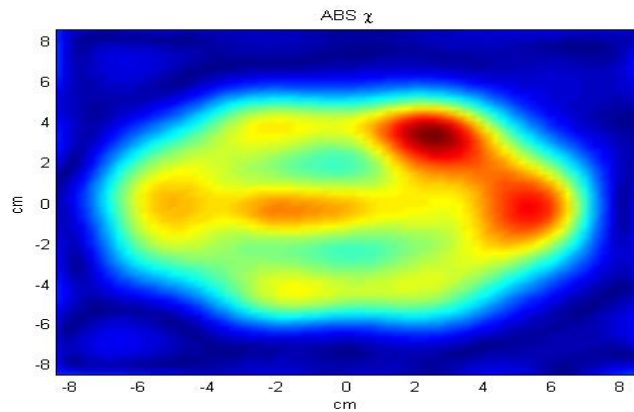


Figure 4.28 : Absolute value of contrast on Microwave imaged by CSI algorithm of the phantom with 500MHz operation frequency and with matching medium $\epsilon_b = 20$

When the operation frequency is increased to 800 MHz, it is impossible to recognize neither the shape of head model nor the blooded region from reconstruction results as shown in Figure 4.29- 4.31.

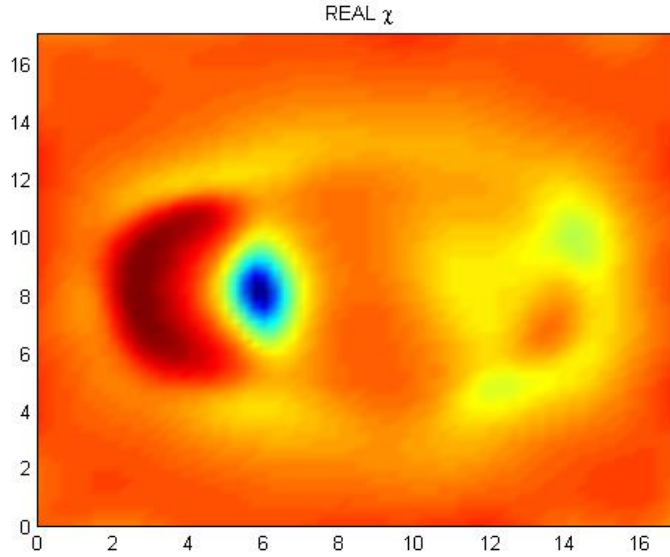


Figure 4.29 : Real part of contrast on Microwave imaged by CSI algorithm of the phantom with 800MHz operation frequency and with matching medium $\epsilon_b = 20$

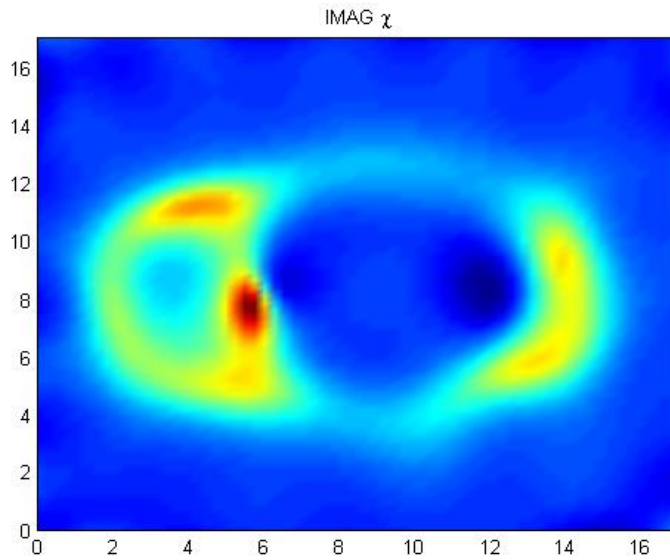


Figure 4.30 : Imaginary part of contrast on Microwave imaged by CSI algorithm of the phantom with 800MHz operation frequency and with matching medium $\epsilon_b = 20$

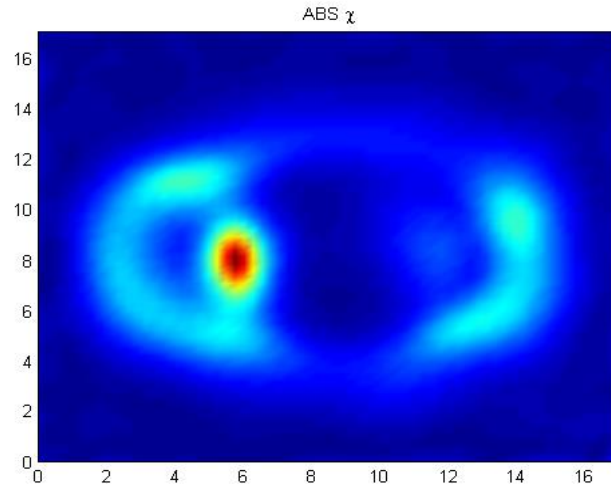


Figure 4.31 : Absolute value of contrast on Microwave imaged by CSI algorithm of the phantom with 800MHz operation frequency and with matching medium $\epsilon_b = 20$

The reconstructions with 1GHz operating frequencies are presented in Figure 4.32-4.34. Although boundary shape of head is appearing, blood region and tissues cannot be recognized.

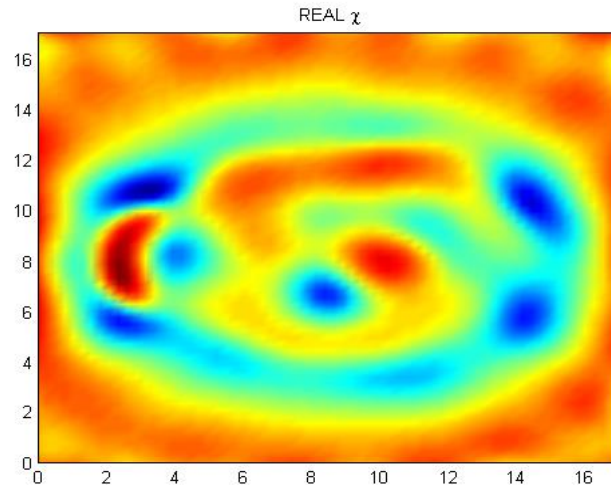


Figure 4.32 : Real part of contrast on Microwave imaged by CSI algorithm of the phantom with 1GHz operation frequency and with matching medium $\epsilon_b = 20$

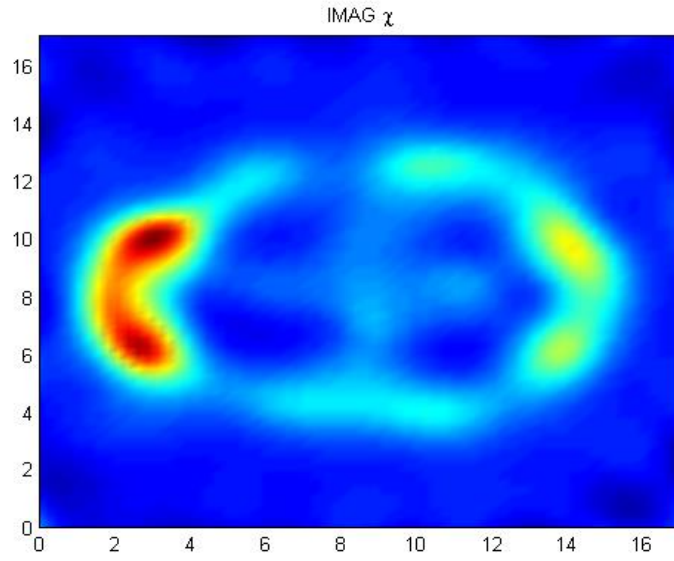


Figure 4.33 : Imaginary part of contrast on Microwave imaged by CSI algorithm of the phantom with 1GHz operation frequency and with matching medium $\epsilon_b = 20$

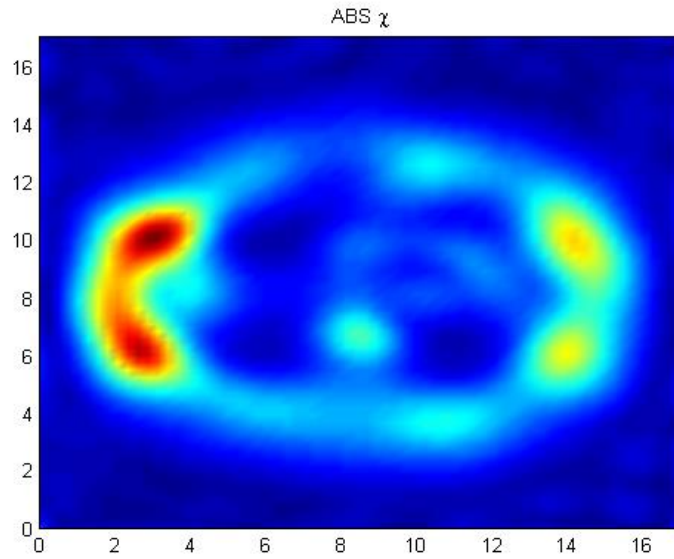


Figure 4.34 : Absolute value of contrast on Microwave imaged by CSI algorithm of the phantom with 1GHz operation frequency and with matching medium $\epsilon_b = 20$

If we investigate the result of reconstructions with 1.2 GHz given in Figure 4.35-4.37, we obtain nearly the same results as 1GHz. We consider that in order to study high frequencies bigger than 1GHz do not improve results.

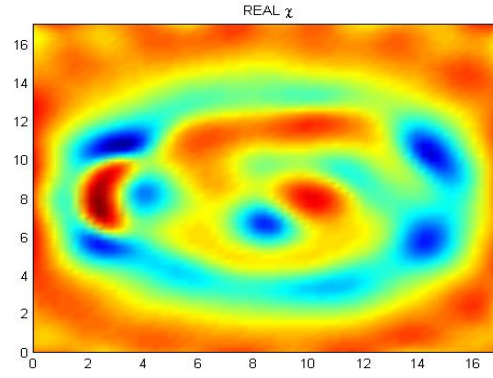


Figure 4.35 : Real part of contrast on Microwave imaged by CSI algorithm of the phantom with 1.2GHz operation frequency and with matching medium $\epsilon_b = 20$

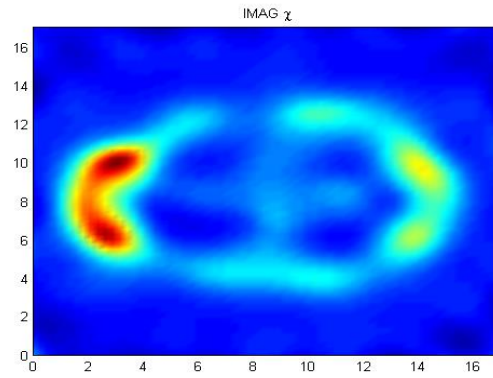


Figure 4.36 : Imaginary part of contrast on Microwave imaged by CSI algorithm of the phantom with 1.2GHz operation frequency and with matching medium $\epsilon_b = 20$

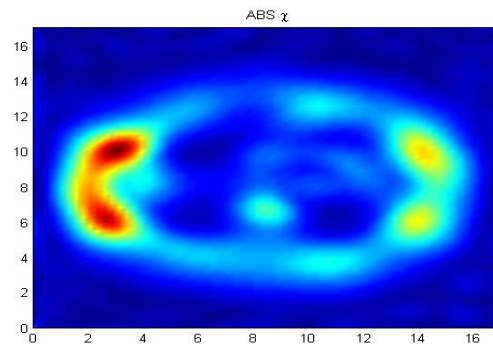


Figure 4.37 : Absolute value of contrast on Microwave imaged by CSI algorithm of the phantom with 1.2GHz operation frequency and with matching medium $\epsilon_b = 20$

To determine the effects of matching medium, the dielectric constant of matching medium is increased to by $\epsilon_b=40$. After reconstruction from scattering field data by CSI method at 500MHz frequency, blooded area is shown with dark red colour in Figure 4.38. Blood region darkest area is centered approximately at the point $x = 10.98\text{cm}$, $y=11.25\text{cm}$. Blood region is detected although it attempts to area where CSF is highly located on reconstructed in Figure 4.37. Imaginary and absolute values of contrast gives explicit results about the location of blood region that is centered approximately at the point $x = 10.9\text{cm}$, $y=12.3\text{cm}$ in Figure 4.39-4.40.

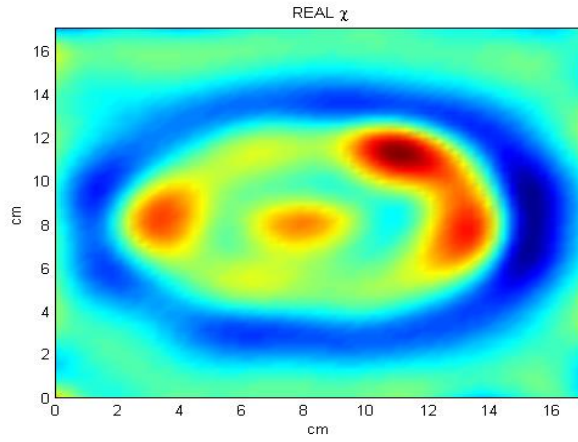


Figure 4.38 : Real part of contrast on Microwave imaged by CSI algorithm of the phantom with 500MHz operation frequency and with matching medium $\epsilon_b = 40$

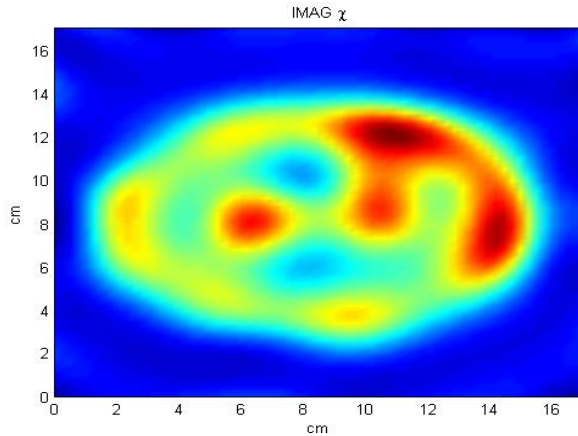


Figure 4.39 : Imaginary part of contrast on Microwave imaged by CSI algorithm of the phantom with 500MHz operation frequency and with matching medium $\epsilon_b = 40$

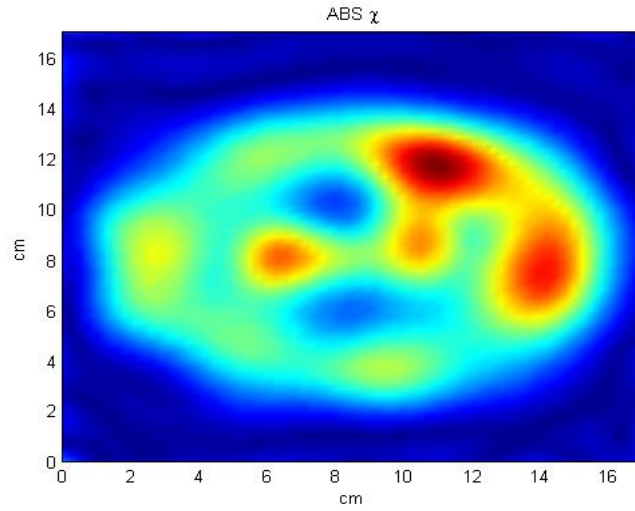


Figure 4.40 : Absolute value of contrast on Microwave imaged by CSI algorithm of the phantom with 500MHz operation frequency and matching medium $\epsilon_b = 40$

When the operation frequency is increased to 800 MHz, size of blood region is getting smaller while being realized of CSF and some other tissues of brain from reconstruction results as shown in Figure 4.41-4.43. Since shape of head is approaching the real dimensions and view, determining the blood region becomes difficultly.

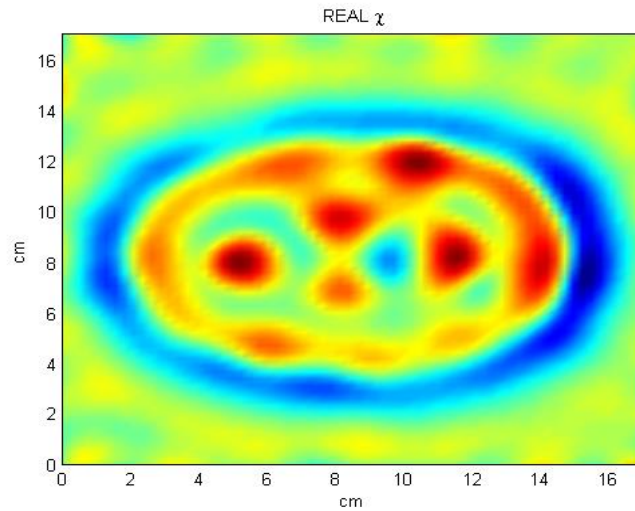


Figure 4.41 : Real part of contrast on Microwave imaged by CSI algorithm of the phantom with 800MHz operation frequency and with matching medium $\epsilon_b = 40$

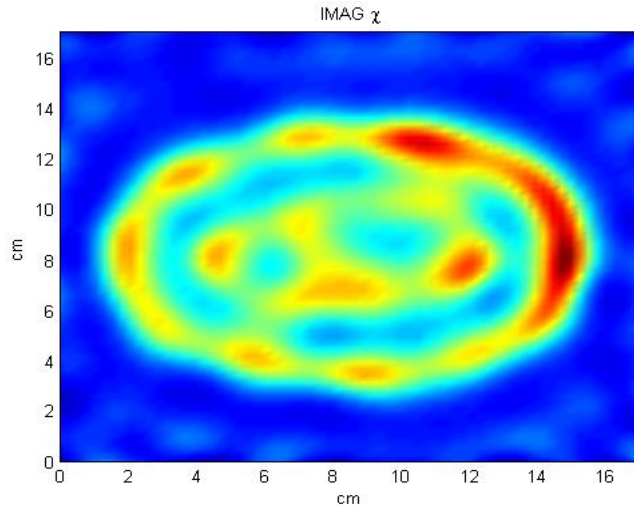


Figure 4.42 : Imaginary part of contrast on Microwave imaged by CSI algorithm of the phantom with 800MHz operation frequency and with matching medium $\epsilon_b = 40$

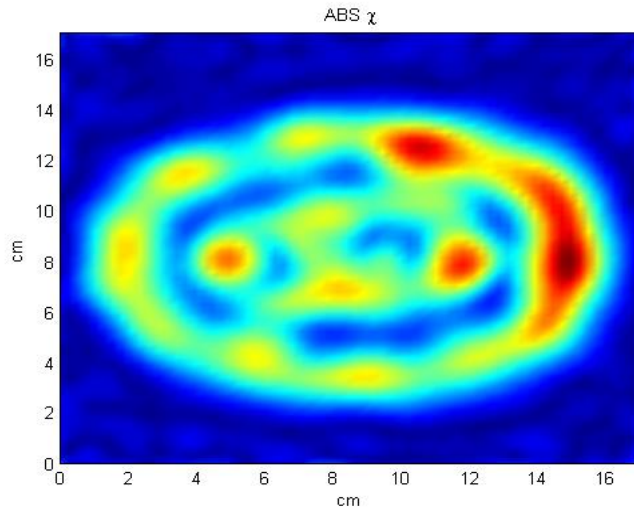


Figure 4.43 : Absolute value of contrast on Microwave imaged by CSI algorithm of the phantom with 800MHz operation frequency and with matching medium $\epsilon_b = 40$

The reconstructions with 1GHz operating frequencies are presented in Figure 4.44-4.46. Blood region is seemed blurred at Figure 4.43 while some tissues near center of the head model is strongly appearance. In this situation, it is not possible to find the location of blood region exactly. Shape of head model and tissues boundaries become distinct.

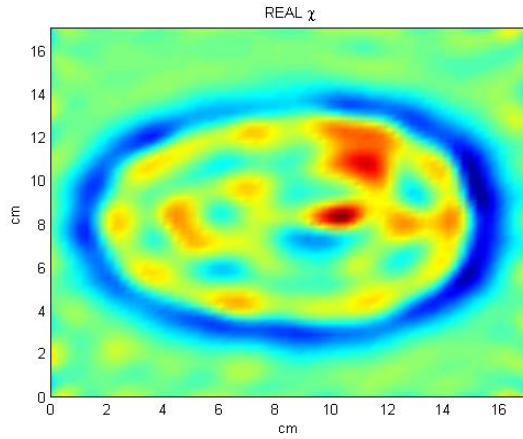


Figure 4.44: Real part of contrast on Microwave imaged by CSI algorithm of the phantom with 1GHz operation frequency and with matching medium $\epsilon_b = 40$

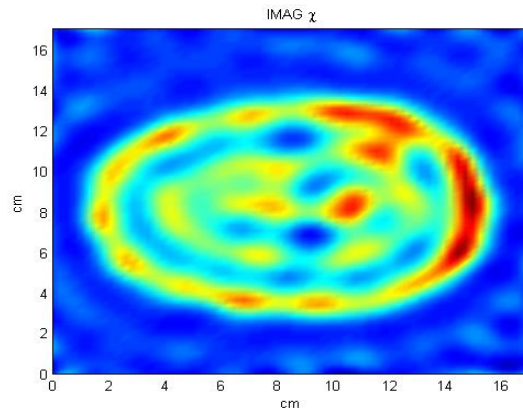


Figure 4.45: Imaginary part of contrast on Microwave imaged by CSI algorithm of the phantom with 1GHz operation frequency and with matching medium $\epsilon_b = 40$

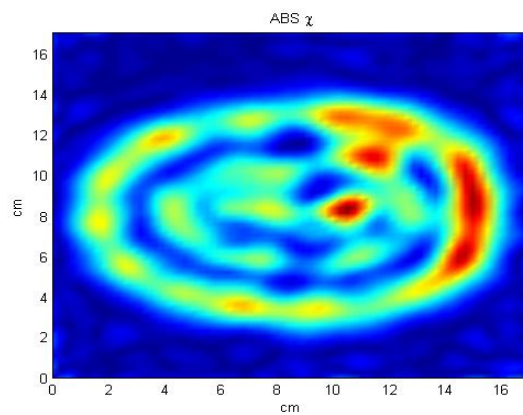


Figure 4.46: Absolute value of contrast on Microwave imaged by CSI algorithm of the phantom with 1GHz operation frequency and with matching medium $\epsilon_b = 40$

The reconstructions with 1.2 GHz operating frequencies are presented in Figures 4.47-4.49. Blood region becomes disappeared at Figure 4.47 while tissues of inside the head model appear clearly. Due to high dielectric constant and conductivity values, CSF is exactly seems. Higher frequencies than 1.2 GHz it is unable to detection the blood region.

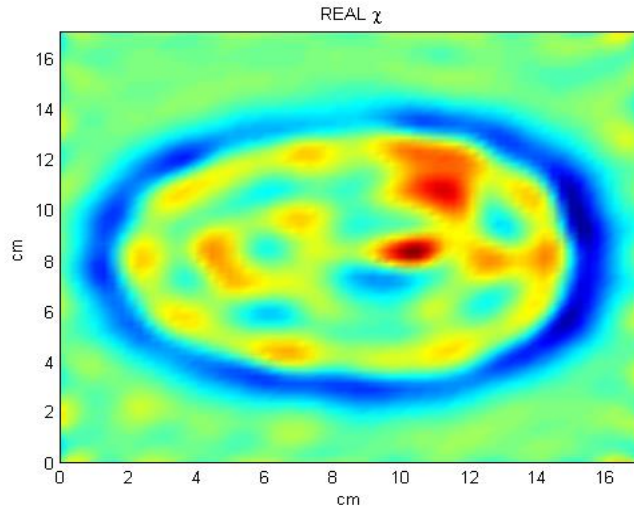


Figure 4.47: Real part of contrast on Microwave imaged by CSI algorithm of the phantom with 1.2GHz operation frequency and with matching medium $\epsilon_b = 40$

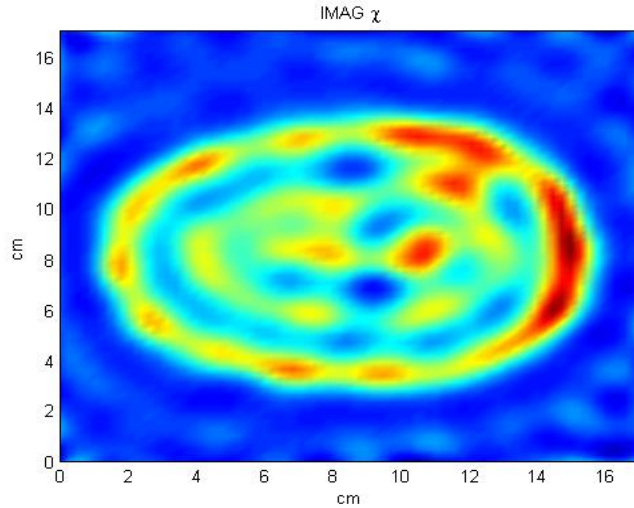


Figure 4.48: Imaginary part of contrast on Microwave imaged by CSI algorithm of the phantom with 1.2GHz operation frequency and with matching medium $\epsilon_b = 40$

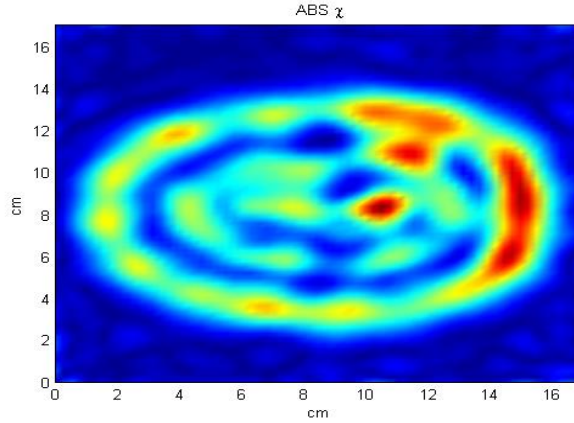


Figure 4.49: Absolute value of contrast on Microwave imaged by CSI algorithm of the phantom with 1.2GHz operation frequency and with matching medium $\epsilon_b = 40$

At last simulation in this topic, to ensure the effects of matching medium, the dielectric constant of matching medium is increased to by $\epsilon_b=60$. After reconstruction from scattering field data by CSI method at 500MHz frequency, blooded area is shown with dark red colour in Figure 4.50. It becomes difficult to detect the blood region due to chosen the matching medium dielectric constant value very closes the blood regions'. Blood region is detected on imaginary and absolute value images of contrast due to high conductivity properties with CSF. Blood region is seen about the location that is centered approximately at the point $x = 10.7\text{cm}$, $y=12.3\text{cm}$ in Figure 4.51-4.52.

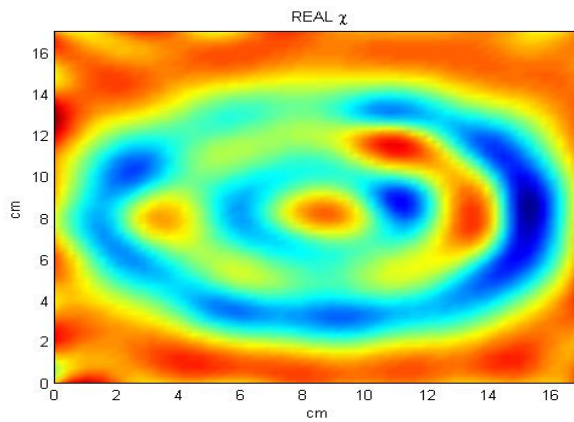


Figure 4.50: Real part of contrast on Microwave imaged by CSI algorithm of the phantom with 500MHz operation frequency and with matching medium $\epsilon_b = 60$

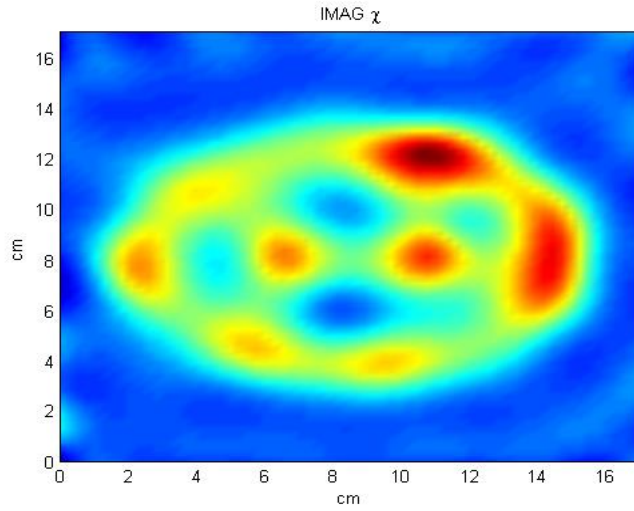


Figure 4.51: Imaginary part of contrast on Microwave imaged by CSI algorithm of the phantom with 500MHz operation frequency and with matching medium $\epsilon_b = 60$

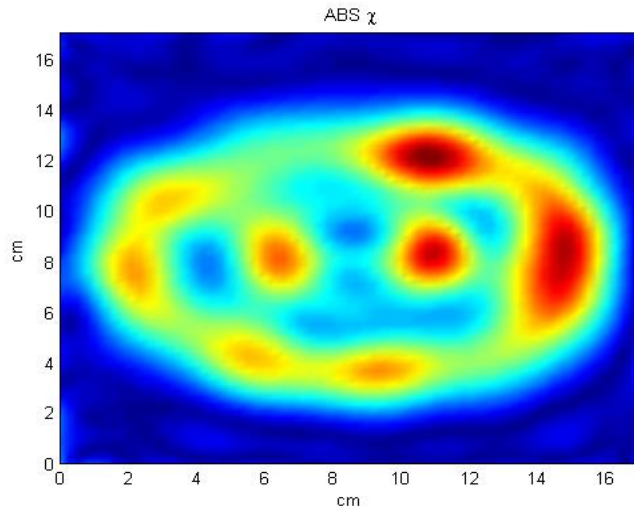


Figure 4.52: Absolute value of contrast on Microwave imaged by CSI algorithm of the phantom with 500MHz operation frequency and with matching medium $\epsilon_b = 60$

At 800MHz operation frequency results as seen on Figure 4.53-4.55 , size of blood region is getting smaller although boundaries of tissues getting sharp due to increasing resolution.

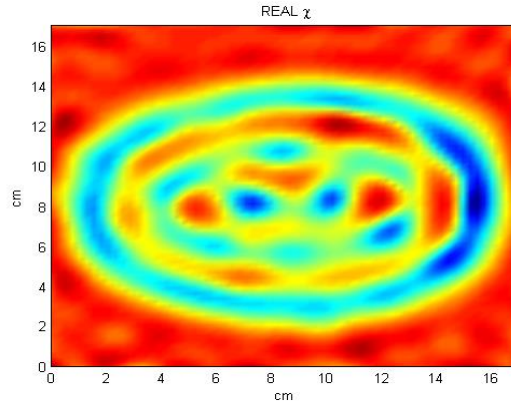


Figure 4.53: Real part of contrast on Microwave imaged by CSI algorithm of the phantom with 800MHz operation frequency and with matching medium $\epsilon_b = 60$

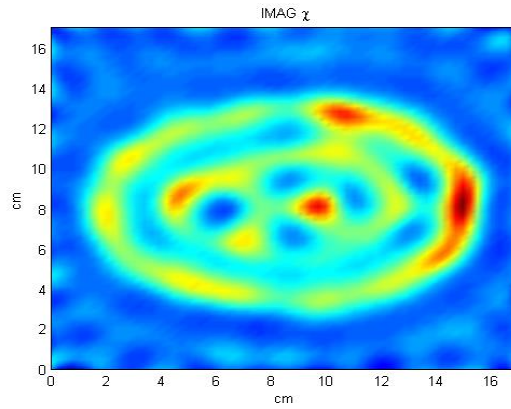


Figure 4.54: Imaginary part of contrast on Microwave imaged by CSI algorithm of the phantom with 800MHz operation frequency and with matching medium $\epsilon_b = 60$

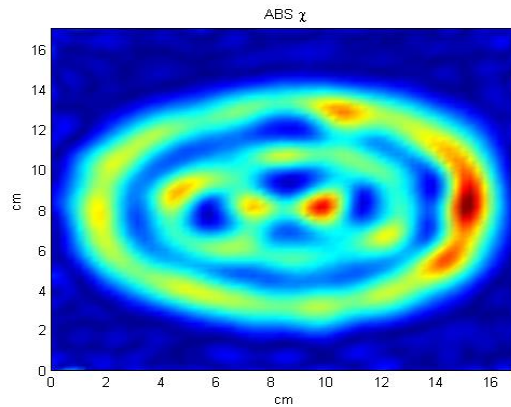


Figure 4.55: Absolute value of contrast on Microwave imaged by CSI algorithm of the phantom with 800MHz operation frequency and with matching medium $\epsilon_b = 60$

High operation frequencies like 1GHz -1.2GHz results as seen on Figure 4.56-4.61 inside of the head model is appearing clearly while there is not any evidence about blood region. The results show that it not meaningful to use higher than 1GHz frequency in order to detect the blood region on the head model. While chosen high frequencies increase the resolution of image of inside the head model, the penetrated electromagnetic fields inside the head model is decreasing.

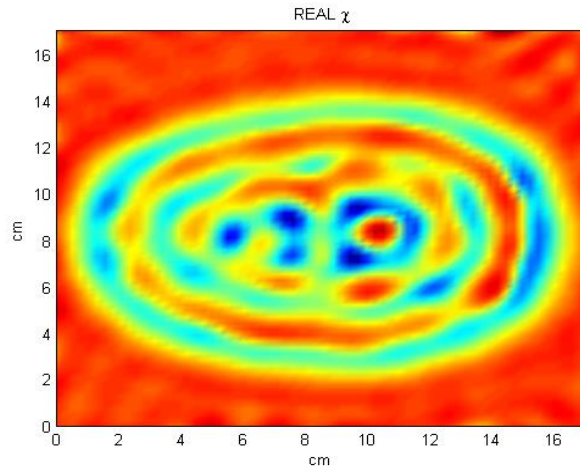


Figure 4.56: Real part of contrast on Microwave imaged by CSI algorithm of the phantom with 1Ghz operation frequency and with matching medium $\epsilon_b = 60$

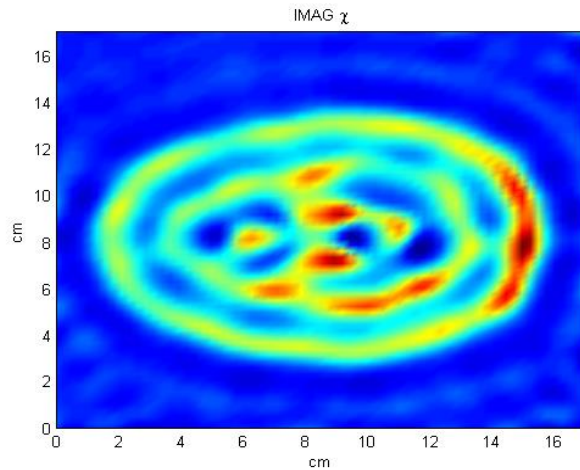


Figure 4.57: Imaginary part of contrast on Microwave imaged by CSI algorithm of the phantom with 1Ghz operation frequency and with matching medium $\epsilon_b = 60$

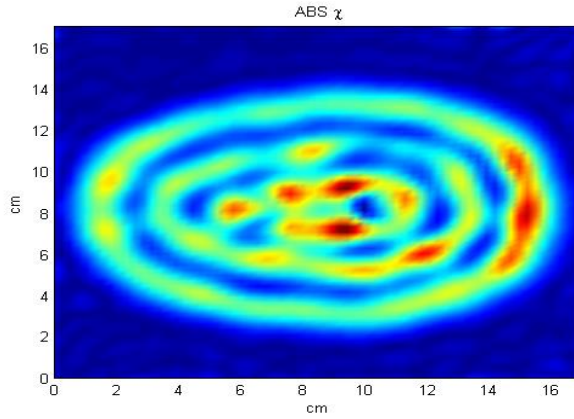


Figure 4.58 : Absolute value of contrast on Microwave imaged by CSI algorithm of the phantom with 1GHz operation frequency and with matching medium $\epsilon_b = 60$

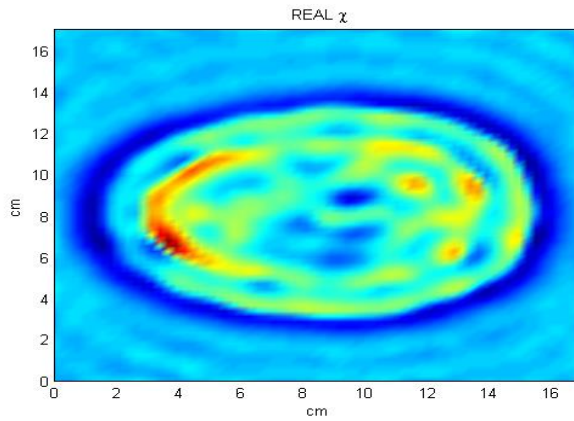


Figure 4.59 : Real part of contrast on Microwave imaged by CSI algorithm of the phantom with 1.2GHz operation frequency and with matching medium $\epsilon_b = 60$

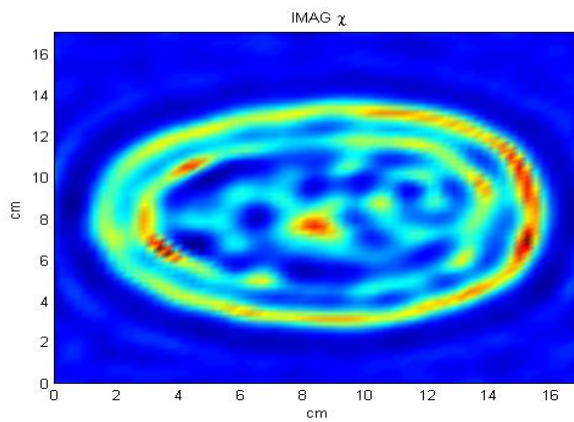


Figure 4.60 : Imaginary part of contrast on Microwave imaged by CSI algorithm of the phantom with 1.2GHz operation frequency and with matching medium $\epsilon_b = 60$

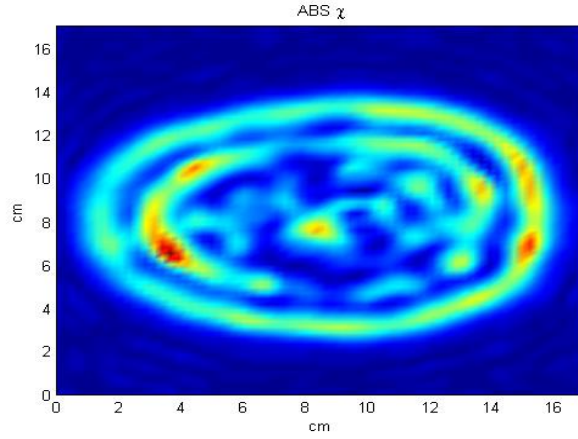


Figure 4.61: Absolute value of contrast on Microwave imaged by CSI algorithm of the phantom with 1.2GHz operation frequency and with matching medium $\epsilon_b = 60$

4.4 Results of Differential Imaging with Contrast Source Algorithm (No Positive Constraint)

Second approach for the detecting of blood region and detecting the changes in the size of the blood region in the stroke affected human brain is microwave imaging by reconstruction from differential scattering field data. The scattered electromagnetic field is synthetically produced via the method of moments in two different time steps. Electrical properties of the head model materials are taken from the Zubal phantom same way as indicated previous section. Four different scenarios growing blood region, decreasing blood region, one region is growing while the other blood region is disappearing and the vice versa condition are simulated.

At first scenario relatively small blood region which size about 1.4cm x 1.4cm rhomb is added to head model as shown in Figure:4.62-4.63. The head model is illuminated with 36 TM polarized line sources, same as previous simulation setups and obtained scattering field data with method of moments. As a realistic scenario, an 30db Additive White Gaussian Noise is added to the scattered field data and scattering field data is record. Following step, same operation is realized for the head model which has two blood regions, one of them is same centered with previous figure but larger size. Difference of two scattering filed data is input parameter of contrast source inversion method in order to scattering field data. The outside region is assumed to be filled by a matching medium with electromagnetic parameters of $\epsilon_b =$

40 and $\sigma_b = 0$ S/m. Same inversion algorithm is used only the input parameter is changed with differential scattering field data. As a result of reconstruction, differential contrast function $\delta\chi(r)$ is obtained.

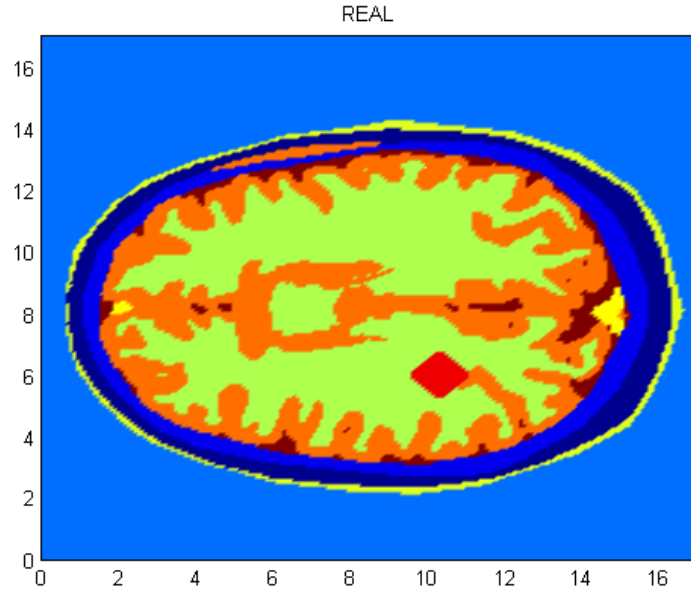


Figure 4.62 : Zubal Phantom model for growing blood regions, real value of the actual contrast function for the first measurement

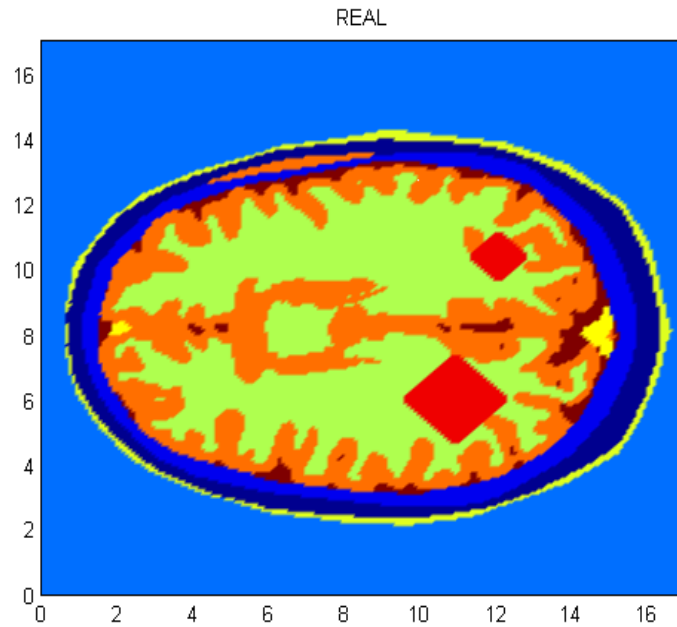


Figure 4.63 : Zubal Phantom model for growing blood regions, real value of the actual contrast function for the second measurement

The reconstructions with 500MHz operating frequencies are presented in Figure 4.64-4.66. Real value of reconstruction differential contrast function does not give any information about the blood regions due to less difference of dielectric constant between the blood region and the materials where same location. High conductivity values of blood rather than the materials where it is located, provides the detection of changing on imaginary and absolute values of reconstruction differential contrast function as shown in Figure 4.65-4.66 .

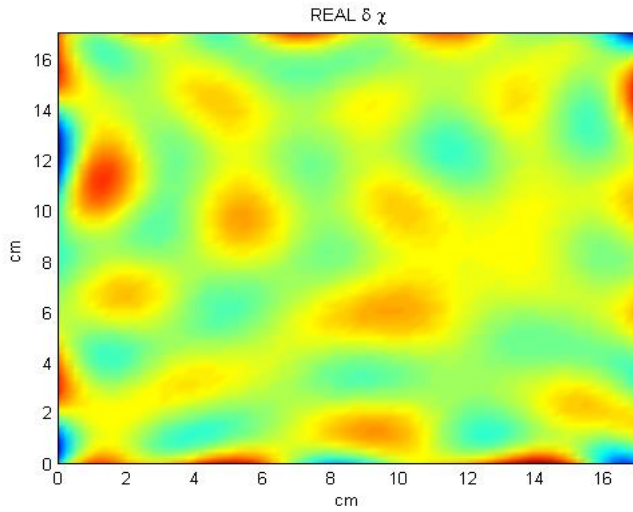


Figure 4.64 : Real value of reconstruction of the differential contrast function $\delta\chi(r)$ in the case of growing blood regions

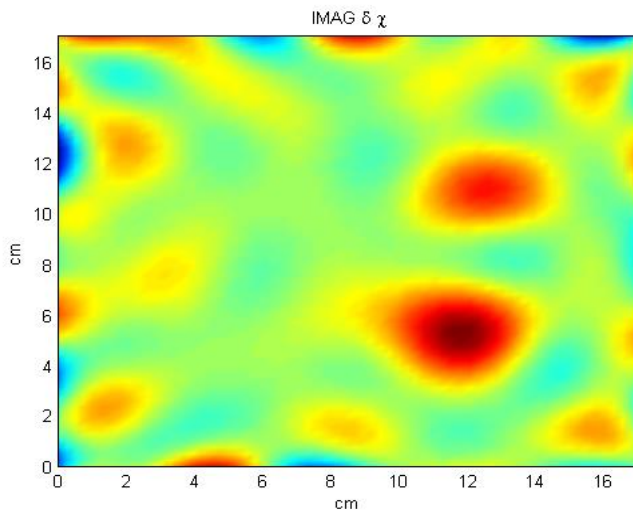


Figure 4.65 : Imaginary value of reconstruction of the differential contrast function $\delta\chi(r)$ in the case of growing blood regions

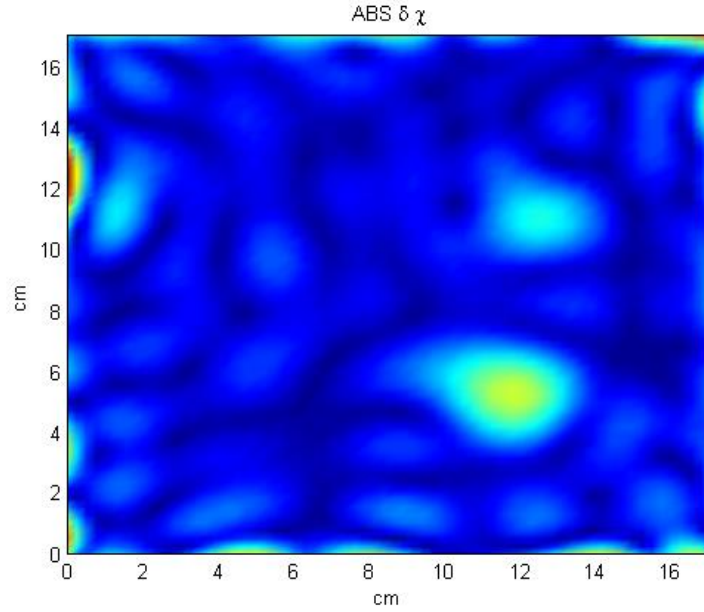


Figure 4.66 : Absolute value of reconstruction of the differential contrast function $\delta\chi(r)$ in the case of growing blood regions

In the second scenario, shrinking blood regions are investigated. Initially, two blood regions which one of them size is about 2.6cm x 2.6.4cm with $x = 10.9$ cm, $y = 6.1$ cm centered, and the other one is about 1.4cm x 1.4cm with $x=12.10$ cm, $y = 10.3$ cm centered, are assumed to be located in the head model. At the second measurement, size of blood, centered at $x = 10.9$ cm and $y=6.1$ cm, is decreased to 1.4cm x 1.4cm. In addition to this, the smaller blood region is disappeared and replaced by healthy region. Real value values as shown in Figure 4.67 of reconstruction differential contrast function does not give any information about the blood regions due to same reasons as indicated previous result. Absolute values of reconstruction differential contrast function as shown in Figure 4.69 same with previous scenario while imaginary values as shown in Figure 4.68 of reconstruction differential contrast function gives negative contrast on blood regions due to replacing healthy tissues with low conductivity values than blood. These results demonstrate that the absolute value of $\delta\chi(r)$ indicates the location of the changes, while the imaginary part shows the nature of the changes.

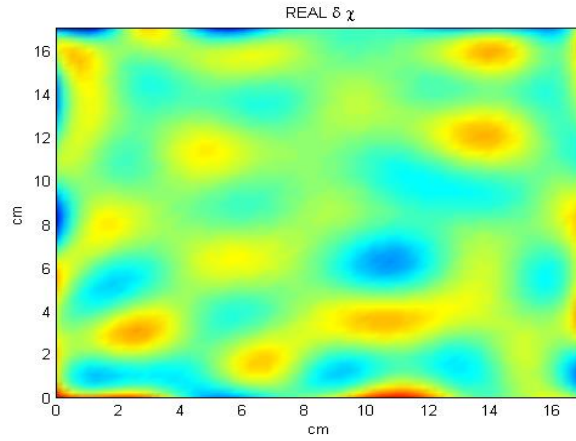


Figure 4.67 : Real value of reconstruction of the differential contrast function $\delta\chi(r)$ in the case of growing blood regions

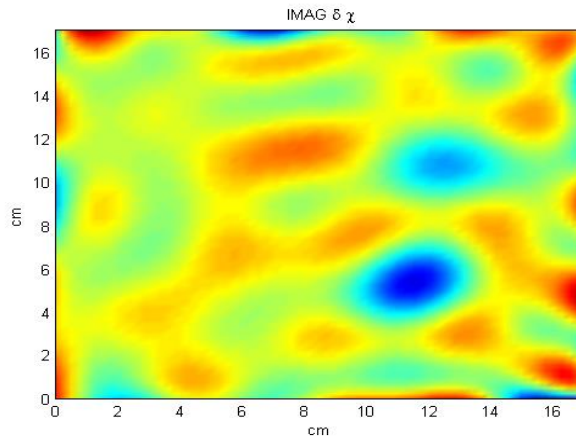


Figure 4.68 : Imaginary value of reconstruction of the differential contrast function $\delta\chi(r)$ in the case of growing blood regions

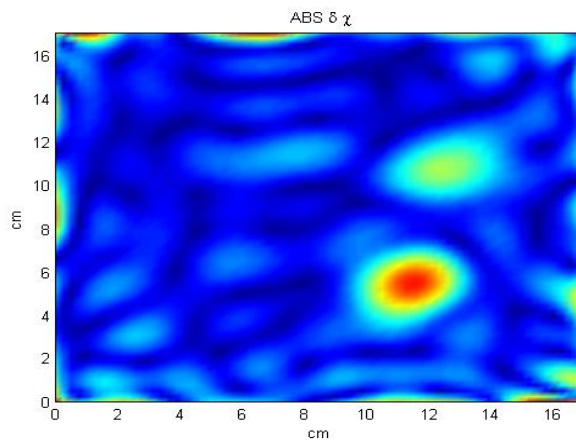


Figure 4.69 : Absolute value of reconstruction of the differential contrast function $\delta\chi(r)$ in the case of growing blood regions

In the third scenario, mixed situation is analyzed. Initially, two blood regions each of them size is about 1.4cm x 1.4cm with $x=10.9$ cm, $y=6.1$ cm and the other is $x=12.10$ cm, $y=10.3$ cm centered, are assumed to be located in the head model as seen in Figure 4.70. At the second measurement, size of blood, centered at $x=10.9$ cm and $y=6.1$ cm, is increased to 2.6cmx2.6cm while the other one is disappeared and replaced with healthy tissues as shown in Figure 4.71. Real value of reconstruction as shown in Figure 4.72 differential contrast function does not give true information about the blood regions location since gives some opinion about the change of blood regions. Absolute values of reconstruction differential contrast function as shown in Figure 4.74 same with previous scenario while imaginary values as shown in Figure 4.73 of reconstruction differential contrast function gives negative contrast on disappearing blood area. On the other hand, at the growing blood region location, reconstruction differential contrast function gives positive contrast. These results demonstrate that the absolute value of $\delta\chi(r)$ indicates the location of the changes, while the imaginary part shows the difference of the changes.

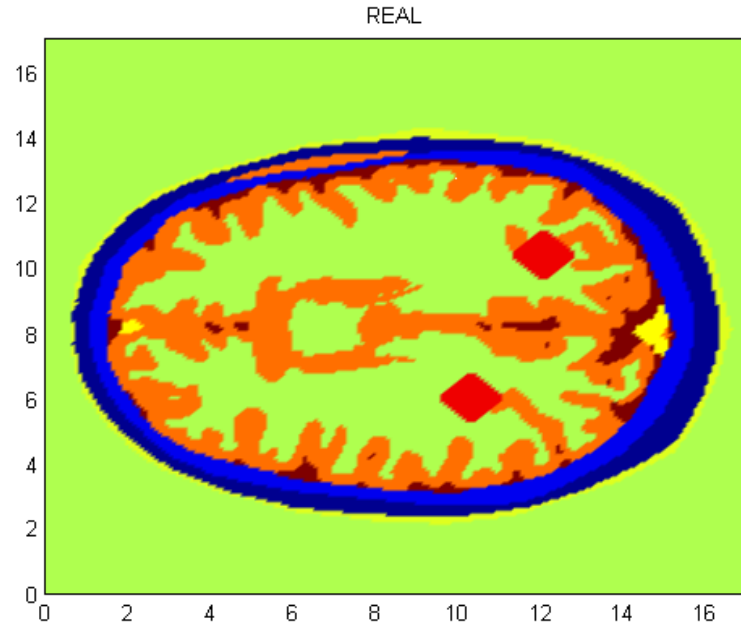


Figure 4.70 : Zubal Phantom model for mixed case, real value of the actual contrast function $\chi(r)$, for the first measurement

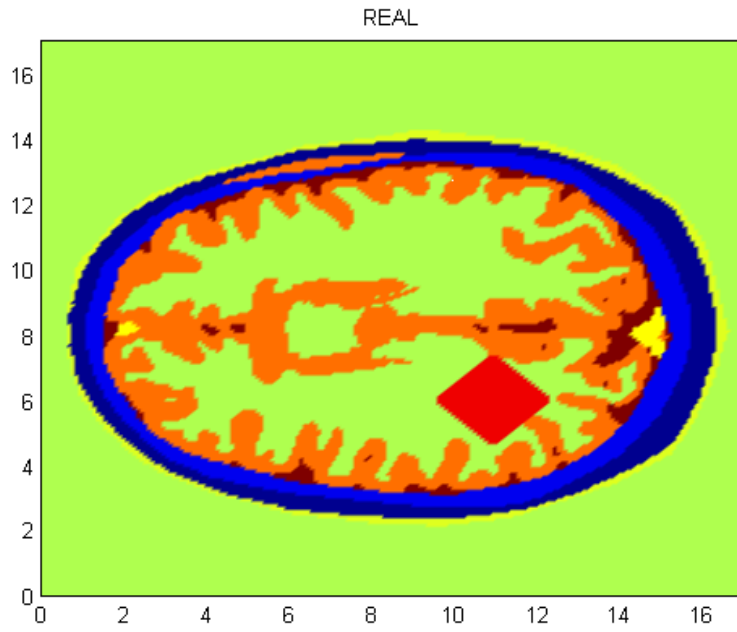


Figure 4.71 : Zubal Phantom model for mixed case, real value of the actual contrast function $\chi(r)$, for the second measurement

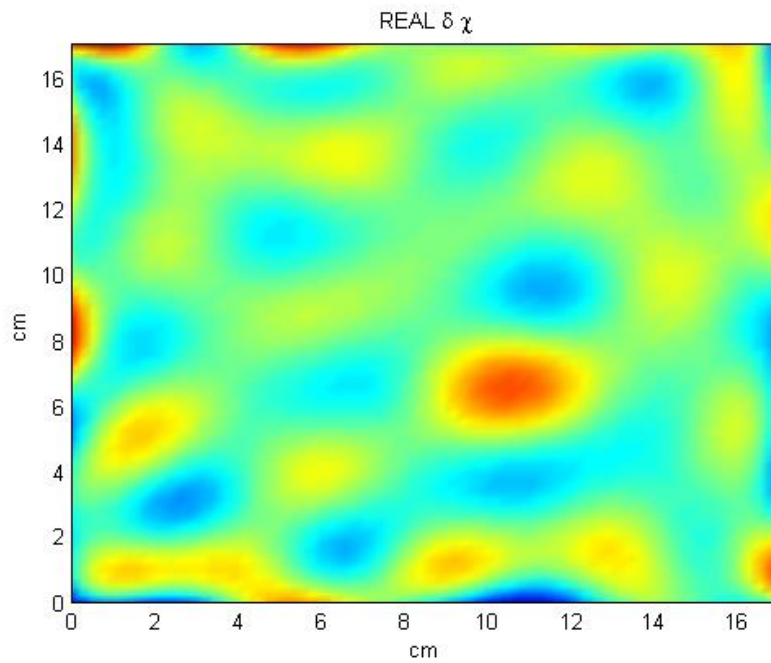


Figure 4.72 : Real value Reconstruction of the differential contrast function $\delta\chi(r)$ for mixed case

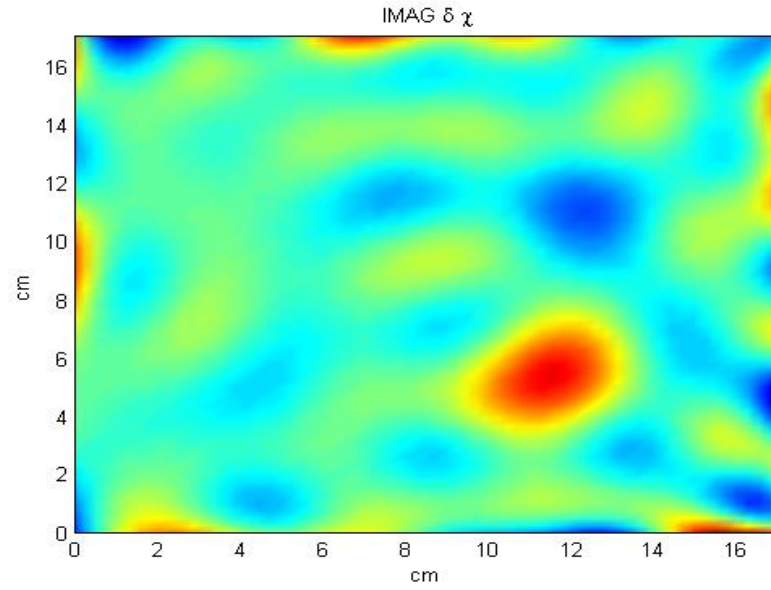


Figure 4.73 : Imaginary value Reconstruction of the differential contrast function $\delta\chi(r)$ for mixed case

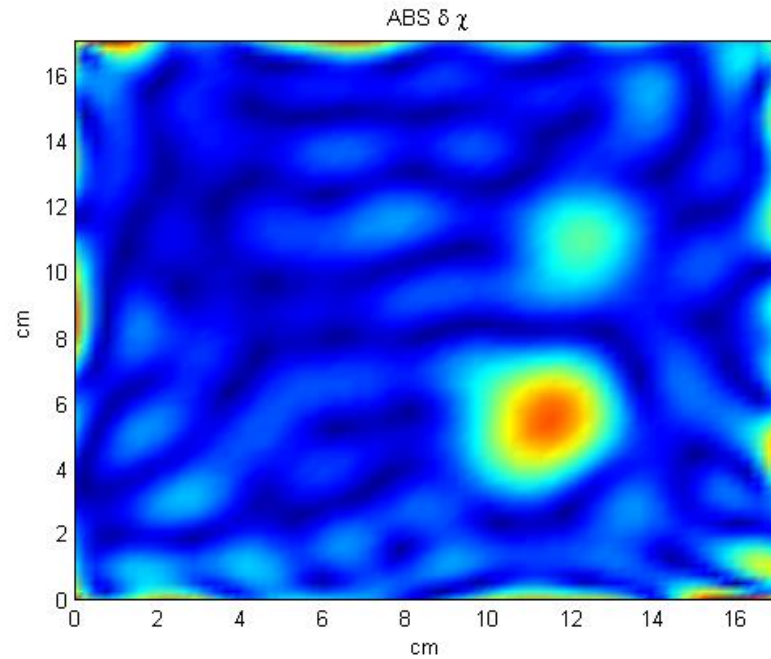


Figure 4.74 : Absolute value Reconstruction of the differential contrast function $\delta\chi(r)$ for mixed case

At last scenario, a situation with blood region does not change is analyzed for determine that the method is prone false alarms or not. Results seen in Figure 4.75 shows that only the effect of noise is apparent and differential contrast function has almost same value everywhere. However results are not given, effects of noise is

analyzed by doing same simulation in different times. Different patterns are observed due to adding random noise at simulation process.

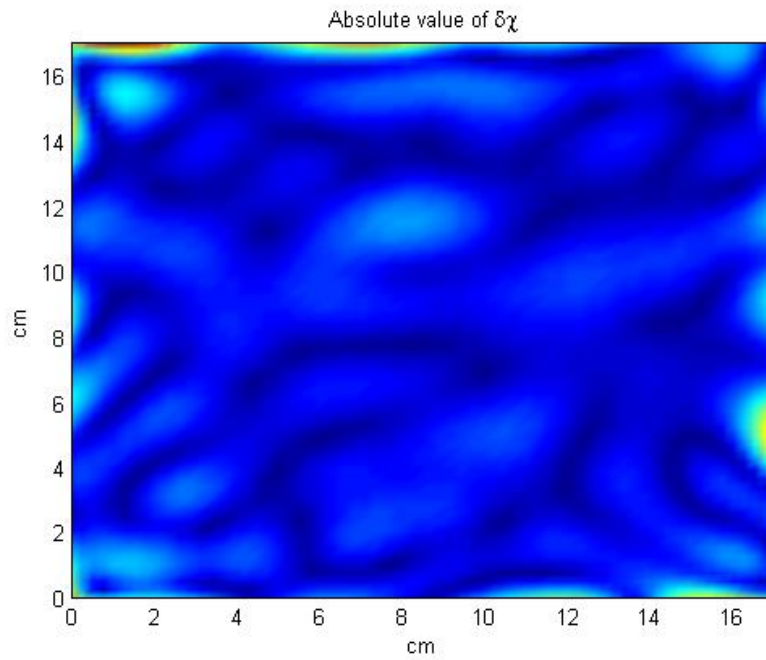


Figure 4.75 : Absolute value Reconstruction of the differential contrast function $\delta\chi(r)$ for static case

5. CONCLUSION

In this thesis, two different approaches are realized for the detecting of blood region and detecting the changes in the size of the blood region in the stroke affected human brain. In the first approach, a microwave imaging technique based on CSI method for the detection of blood region within a realistic human brain model is tested. Various simulations with different operating frequencies and matching media have been performed. The result show that the CSI method with positive constraint is efficient of reconstructing reasonably large blood regions within a realistic human brain provided that optimal values of operating frequency and matching medium are chosen. At low frequencies like 500Mhz, the shapes and the locations of the blood regions cannot be determined accurately due to the low resolution at these frequencies. Furthermore, the shape of head cannot be reconstructed completely. At higher frequencies such as 800 MHz, more accurate information about the shape and the size of blood region is obtained. On the other hand, although the shape of human brain becomes more clearly depicted at working frequencies above 1 GHz, the detection of blood regions becomes harder. Moreover, detection becomes virtually impossible for the frequencies above 1.2 GHz.

The results also demonstrate the importance of the matching medium. It is clearly observed that without matching medium the method fails to produce useful results due to the high contrast between the air and the human head. High contrast causes a significant reflection on the interface, and impedes the penetration of the electromagnetic field into the inner regions of the human brain. Another important observation is the effect of positivity constraint on the success of CSI algorithm. For higher values of dielectric parameter of the matching medium, the positivity constraint ceases to be physically correct. Nevertheless, using positive constraint improves the detection of blood region, albeit it causes a deformation in the reconstruction of the tissues such as skin, skull or fat. This is an expected result considering that the positivity constraint is invalid for these tissues.

The high conductivity of the cerebrospinal fluid makes the detection of the blood regions more difficult. Since the imaginary part of the contrast is affected by the conductivity, it cannot be used to distinguish blood regions from the cerebrospinal fluid CSF. Especially when the positivity constraint is absent, the CSF strongly affects the quality of the reconstruction. Although meaningful results are obtained for the operating frequency of 500 MHz; for 800 MHz and above, it becomes impossible to detect the blood regions. It has been also observed that for frequencies higher than 1 GHz, the effect of CSF becomes more dominant, and it supersedes the blood regions in the reconstructed profile. Nevertheless, it can be concluded that the method is capable of detecting reasonably large blood regions for optimal operating frequencies, and matching medium.

Second approach for detecting the changes in the sizes of the blood regions in the stroke affected human brain is the differential microwave imaging. For this case, the scattered electromagnetic field is assumed to be measured in two different time steps. The numerical simulations show that for growing blood region, a positive contrast difference occurs on the location of blood region. On the other hand, for shrinking blood region, a negative contrast difference is observed. These results demonstrate that the method indicates the locations and types of changes in the blood regions with accuracy. However, similar to the case with full reconstruction, the results strongly depend on the operating frequency. Above 1 GHz, detection of the blood region and its changes of size become impossible. Furthermore, it has been observed that the dielectric constant of matching medium affects the outcome by causing variations in the location and the values of contrast difference areas. With optimal values of dielectric constant of matching medium, detecting relatively small blood regions is possible even with realistic noise levels. In addition, in the case of no change, the method produces a homogeneous reconstruction. Therefore, it can be concluded that the method is especially suitable for continuous monitoring.

The results can be further enhanced by using different inversion algorithms for differential imaging. Finally, in the future, in order to improve the performance of the method, frequency-hopping techniques can be inserted to CSI algorithm. Also using experimental data as the solution of the forward problem would make the tests more robust and more realistic. This will require using antennas instead of ideal line sources. It should be noted that, for realistically applications, the coupling effects

between the antennas and the dielectric losses in the matching medium must be considered. In addition, a suitable measurement setup must be designed in order to use the antennas within a liquid matching medium. Finally, as an additional theoretical study, the CSI based inversion scheme can be generalized to 3-D models to improve the quality of the reconstruction.





REFERENCES

- [1]Chandra, **R.**, Zhou, **H.**, Balasingham **I.** and Narayanan, **R. M.** (2015). On the Opportunities and Challenges in Microwave Medical Sensing and Imaging. *IEEE Transactions on Biomedical Engineering.* 62, 7, 1667 – 1682.
- [2]Semenov, **S.** (2009) Microwave tomography: Review of the progress towards clinical applications *Philos. Trans. A Math. Phys. Eng. Sci.* 3021–3042.
- [3]Scapaticci, **R.**, Di Donato **L.**, Catapano **I.**, and Crocco **L.** (2012). A feasibility study on microwave imaging for brain stroke monitoring. *Progress In Electromagnetics Research B.* 40, 305–324.
- [4]Semenov, **S. Y** and Corfield, **D. R.** (2008). Microwave tomography for brain imaging: Feasibility assessment for stroke detection. *International Journal of Antennas and Propagation.* , 2008
- [5]Fhager, **A** and Persson, **M.** (2012). Stroke detection and diagnosis with a microwave helmet, in EuCAP 2012, in *Proceedings of 6th European Conference on Antennas and Propagation*, Prague, 26-30 March
- [6]Nikolova, **N. K.** (2011). Microwave imaging for breast cancer. *IEEE Microw.Mag.*, 12, 7, 78–94.
- [7]Meaney, **P. M.** (2012). Clinical microwave tomographic imaging of the calcaneus: A first-in-human case study of two subjects. *IEEE Trans.Biomed. Eng.*, 59,12, 3304–3313
- [8]Semenov, **S.**(2006) Microwave tomography: Microwave tomographic imaging of the heart in intact swine. *J. Electromag. Waves Appl.* 20, 7, 3021–3042.
- [9]Colton, **D.** and Kirsch, **A.** (1996). A simple method for solving inverse scattering problems in the resonance region. *Inverse Problems.* 12, 383–393.
- [10]Kirsch, **A.** (1998). Characterization of the shape of a scattering obstacle using the spectral data of the far field operator. *Inverse Problems.* 14, 1489.
- [11]Roland, **P.** (1996). Inverse scattering: A fast new method to solve inverse scattering problems. *Inverse Problems.* **12**, 731.
- [12]Joachimowicz, **N.** (1991). Inverse scattering: An iterative numerical method for electromagnetic imaging. *IEEE Trans. Antennas Propag.* 39, 12, 1742–1753.

- [13]**Franchois, A. and Pichot, C.** (1991). Microwave imaging-complex permittivity reconstruction with a Levenberg-Marquardt method. *IEEE Trans. Antennas Propag.* 45, 2, 203-215.
- [14]**Chew, W.C. and Wang, Y. M.** (1990). Reconstruction of two-dimensional permittivity distribution using the distorted born iterative method. *IEEE Trans. Med. Imag.* 9, 2, 218-225.
- [15]**Ireland, D.** (2013). Microwave imaging for brain stroke detection using Born iterative method. *IET Microw. Antennas Propag.* 7, 11, 909-915.
- [16]**Mustafa, S.** (2013). Novel preprocessing techniques for accurate microwave imaging of human brain. *IEEE Antennas Wireless Propag.* 12, 460–463.
- [17]**Mohammed, B. J.** (2014). Microwave system for head imaging. *IEEE Trans. Instrum. Meas.* 63, 1, 117–123.
- [18]**Semenov, S. Y., Bulyshev, A. E., Abubakar, A., Posukh, V. G., Sizov, Y. E., Souvorov, A. E., van den Berg, P. M. and Williams T. C.** (2005). Microwave-Tomographic Imaging of the High Dielectric-Contrast Objects Using Different Image-Reconstruction Approaches:. *IEEE Transactions on Microwave Theory and Techniques.* 53, 7, 2284 - 2294.
- [19]**Abubakar, A., van den Berg, P. M. and Mallorqui, J. J.** (2002). Imaging of Biomedical Data Using a Multiplicative Regularized Contrast Source Inversion Method *IEEE Transactions on Microwave Theory and Techniques.* 50, 7, 1761 – 1771.
- [20]**Scapaticci, R., Bucci, O., Catapano, I., and Crocco, L.** (2014). Differential microwave imaging for brain stroke followup. *International Journal of Antennas and Propagation.* 2014,
- [21]**Bjelogric, M., Fuchs, B. and Mattes, M.** (2016). Contributions to 3d differential microwave imaging, in EuCAP 2016, in *10th European Conference on Antennas and Propagation*, Davos, 10-15 April
- [22]**Guardiola, M., Jofre, L., Capdevila, S. and Romeu, J.** (2012). Uwb brain differential imaging capabilities, in EUCAP 2012, in *6th European Conference on Antennas and Propagation*, Prague, 26-30 March.
- [23]**Van Den Berg, P. M. and Kleinman, R. E.** (1997). A contrast source inversion method, *Inverse problems.* 13, 6, 1607.
- [24]**Richmond, J.H.** (1965). Scattering by a dielectric cylinder of arbitrary crosssection shape *IEEE Transactions on Antennas and Propagation* .13, 3, 334 – 341.
- [25]**Engl, Heinz Werner, Hanke, Martin, Neubauer, A.** (2000). *Regularization of Inverse Problems.* Springer Netherlands.
- [26]**Van Den Berg, P. M., Broekhoven, A.L. and Abubakar, A.** (1999). Extended contrast source inversion, *Inverse problems.* 15, 5, 1325.
- [27]**Van Den Berg, P. M.** (1999). Nonlinear Scalar Inverse Scattering: Algorithms and Application *Inverse problems.* 141.

- [28] **Zubal, I. G., Harrell, C. R., Smith, E. O., Rattner, Z., Gindi, G. and Hoffer, P. B.** (1994). Computerized three-dimensional segmented human anatomy *Medical physics*. 21, 2, 299–302.
- [29] **Ireland, D and Abbosh, A. M.** (2012). Optimised second-order Debye parameters for head tissues at microwave frequencies at the Antennas and Propagation Society Int. Symp., Chicago, IL,



CURRICULUM VITAE



Name Surname : İSMAİL DİLMAN
Place and Date of Birth : BURSA / 23.03.1986
E-Mail : dilman@itu.edu.tr

EDUCATION :

- **B.Sc.** : 2009, Yıldız Technical University, Electric-Electronic Faculty, Electronic and Communication Engineering

PUBLICATIONS, PRESENTATIONS AND PATENTS ON THE THESIS:

- **Dilman İ., Yildirim U., Bilgin, E., Semih D., Mehmet C. and Akduman İ.** 2016: I. Dilman, U. Yildirim, S. Cosgun, S. Dogu, M. Cayoren, and I. Akduman, "Feasibility of brain stroke imaging with microwaves," in Asia-Pacific Conference on Applied Electromagnetics. IEEE, 2016, Langkawi
- **Yildirim U., Dilman İ., Bilgin, E., Semih D., Mehmet C. and Akduman İ.** 2016: Continuous Monitoring of Hemorrhagic Brain Strokes via Contrast Source Inversion, EUCAP 2016 , Paris (Under review)